ANALYSIS AND DESIGN OF QUIET HYPERSONIC WIND TUNNELS

BY HADASSAH NAIMAN

A dissertation submitted to the

Graduate School—New Brunswick

Rutgers, The State University of New Jersey

in partial fulfillment of the requirements

for the degree of

Doctor of Philosophy

Graduate Program in Mechanical and Aerospace Engineering

Written under the direction of

Doyle D. Knight

and approved by

_____

_____

_____

_____

New Brunswick, New Jersey

January, 2010

ABSTRACT OF THE DISSERTATION

ANALYSIS AND DESIGN OF QUIET HYPERSONIC WIND TUNNELS

by HADASSAH NAIMAN

Dissertation Director: Doyle D. Knight

The purpose of the present work is to integrate CFD into the design of quiet hypersonic wind tunnels and the analysis of their performance. Two specific problems are considered. The first problem is the automated design of the supersonic portion of a quiet hypersonic wind tunnel. Modern optimization software is combined with full Navier-Stokes simulations and PSE stability analysis to design a Mach 6 nozzle with maximum quiet test length. A response surface is constructed from a user-specified set of contour shapes and a genetic algorithm is used to find the "optimal contour", which is defined as the shortest nozzle with the maximum quiet test length. This is achieved by delaying transition along the nozzle wall. It is found that transition is triggered by Goertler waves, which can be suppressed by including a section of convex curvature along the contour. The optimal design has an unconventional shape described as *compound curvature*, which makes the contour appear slightly wavy.

The second problem is the evaluation of a proposed modification of the test section in the Boeing/AFOSR Mach 6 Quiet Tunnel. The new design incorporates a section of increased diameter with the intention of enabling the tunnel to start in the presence of larger blunt models. Cone models with fixed base diameter (and hence fixed blockage ratio) are selected for this study. Cone half-angles from 15° to 75° are examined to ascertain the effect of

the strength of the test model shock wave on the tunnel startup. The unsteady, laminar, compressible Navier-Stokes equations are solved. The resulting flowfields are analyzed to see what affect the shocks and shear layers have on the quiet test section flow. This study indicates that cone angles $\leq 20^\circ$ allow the tunnel to start.

Keywords: automated optimization, response surface, parabolized stability equations, compound curvature, laminar, wind tunnel, unstart, test section

Acknowledgements

I am very grateful to my advisor Prof. Doyle Knight for his technical guidance, moral support and endless patience.

I owe a special thanks to our system administrator Alexei Kotelnikov for his consistent help with installing and running all of the new programs I used for this thesis.

I wish to acknowledge Dr. Heath Johnson from University of Minnesota, for his help installing and running STABL and analyzing my results. I would also like to acknowledge Dr. Chau-Lyan Chang from NASA Langley Research Center, for allowing me to run LASTRAC and analyzing my results. Thank you both for your patience in answering my many (long!) emails; this training has been an invaluable asset.

This research was supported by AFOSR grant FA9550-06-1-0195.

Table of Contents

List of Tables

List of Figures

Chapter 1

Introduction

One of the major challenges in hypersonic flow research is the accurate prediction of transition. The location and extent of laminar-turbulent transition is a critical parameter in hypersonic vehicle design. Transition location affects estimates of aerodynamic heating, skin friction drag, and other boundary layer properties. Computations of laminar heat transfer can be made with good accuracy; in many cases, the largest uncertainty in calculating the total heat flux to a vehicle results from the estimate of transition location [5].

Transition experiments have been carried out in conventional ground testing facilities for decades. However, most of the experimental data obtained from these facilities are contaminated by the high levels of noise that radiate from the turbulent boundary layers normally present on the nozzle walls. The effects of this acoustic noise are profound. These high noise levels can cause transition to occur at Reynolds numbers that are an order of magnitude earlier than in flight [6]. Not only is the location of transition affected, but the parametric trends for transition can also be dramatically different from those in flight [7].

Quiet flow wind tunnels have been developed to simulate hypersonic flow in flight, where the noise levels are very low. A quiet wind tunnel requires a laminar boundary layer on the test section walls; a turbulent boundary layer would generate acoustic fluctuations in the test section core flow. A review of the various efforts worldwide to develop quiet tunnels is provided in reference [8]. A quiet Mach-3.5 tunnel was the first to be successfully installed at NASA Langley in the early 1980s. This was followed by a quiet Mach-6 hypersonic facility in the mid-1990s. Unfortunately, this nozzle was removed from service due to a space conflict, and is now being reinstalled at Texas A&M. The Boeing/AFOSR Mach-6 Quiet Tunnel (BAM6QT) at Purdue University was constructed during 1995-2001. It was developed to provide laminar nozzle-wall boundary layers at high Reynolds numbers, and thus low noise

levels comparable to flight. It is, at present, the only operational hypersonic quiet tunnel anywhere in the world [9].

This investigation focuses on two major issues related to the achievement of high Reynolds number quiet flow in hypersonic tunnels: 1) automated optimal design of quiet hypersonic tunnels, and 2) tunnel startup in the presence of blunt models. In the former case, a fully automated design methodology is developed to determine the optimal shape of the supersonic nozzle to achieve laminar flow on the nozzle walls and maximize the quiet flow test section size. Chapter 3 describes the automated procedure which replaces the conventional trial-and-error approach. In the latter case, detailed time-accurate numerical simulations are performed for a cone model of different angles to demonstrate the limiting size of the model that permits tunnel startup. A proposed tunnel modification is evaluated to determine if it will allow larger, blunt models to be started. Results are presented in chapter 7. For both problems, the BAM6QT configuration conditions are used because of its uniqueness.

1.1 Literature Review

1.1.1 Transition Analysis

Boundary layer transition is the process by which a laminar boundary layer becomes turbulent. While the intricacies of this process are not fully understood at present, certain features have become clear, and it is known that the process proceeds through a series of stages. The initial stage of the natural transition process is the "receptivity stage" where external disturbances in the outer freestream flow, such as freestream turbulence, surface roughness or acoustic noise, are transformed into internal instability oscillations within the boundary layer. Upon entering the boundary layer, a wide spectrum of disturbances is present. Many of these disturbances decay; however, a limited number become amplified with further downstream development.

The second stage of transition is the exponential growth of these few unstable disturbances. Linear Stability Theory (LST) describes it by following the most unstable mode. It is generally accepted that for subsonic incompressible boundary layers, these initial instabilities will cause transition and ultimately lead to turbulent flow, taking the form of

Tollmien-Schlichting waves. The third stage is triggered when the amplitudes of the disturbances become large enough to introduce nonlinear effects. At this stage, the uniform spanwise mean flow becomes modulated by the nonlinear interaction of the disturbances and the boundary layer thickness can vary strongly in the streamwise direction.

Boundary layer disturbances amplify through one or more of many possible mechanisms, including first and second mode amplification, roughness-induced transition, crossflow vortices and Goertler instabilities. Different mechanisms dominate under various conditions. An important part of predicting transition in boundary layers is understanding the different mechanisms that drive the transition to turbulence. Numerous reviews and workshops have focused on the critical ideas of transition modeling via experiments [10], linear theory [11], parabolized equations [12] and direct numerical simulations [13]. A review of stability mechanisms in 3D boundary layers is provided in reference [14]. The study of 3D boundary layers is motivated by the need to understand the fundamental stability mechanism that causes transition on swept wings.

Mack [15] performed an extensive numerical investigation of the linear stability characteristics of compressible laminar boundary layers and discovered some major differences between incompressible and compressible theories. He showed that for a flat plate at supersonic Mach numbers up to about four, the laminar boundary layer is unstable to what he called *first mode disturbances*. These are the compressible counterpart of Tollmien-Schlichting waves, except that they are most unstable when aligned at an oblique angle of $50° - 60°$. At Mach numbers above that range, a *second mode* of instability appears. The second mode can be thought of as a trapped acoustical wave that is most amplified when it is two-dimensional. Second mode waves are destabilized to a moderate extent by wall cooling, whereas first mode waves are destabilized by heating. In general, he found that whenever the relative flow is supersonic over some portion of the boundary layer profile there are an infinite number of waves for a single phase velocity. These additional disturbances are called higher modes. Numerous studies have investigated these higher modes, particularly the second mode, in supersonic and hypersonic flow [16, 17, 18]. The amplification rates for higher modes are always lower than those of the first two modes and are therefore not responsible for transition [15].

A given disturbance frequency cannot be characterized as being of the first or second mode [15]. The mode identification depends on the Reynolds number, and the same frequency can be both a first and second mode disturbance at different Reynolds numbers. Wave speed is used to classify instabilities based on their velocity relative to the edge. This requires an accurate determination of the edge location.

Numerous transition models have been developed over the years and implemented within CFD codes. These range from simple algebraic models like Baldwin Lomax to the standard two equation models like k-epsilon that are included in most commercial flow solvers. These are primarily used to model the effect of the transition region on such quantities as skin friction and heat transfer [19]. However, in all these models the starting location of transition is given and the flow solver essentially has some sort of flag that turns the model on when transition is assumed to have occurred. The business of *predicting* this location a priori is left to experiments, correlations or stability analysis.

Stability analysis can be divided into two categories: Linear Stability Theory (LST) and theory based on the Parabolized Stability Equations (PSE). Linearity implies that there is no interaction between the mean flow and the disturbances. The fluctuating disturbance is assumed to be small compared to the mean flow, such that higher order fluctuating terms are neglected and the resulting equations are linear. LST employs the parallel flow assumption, which states that the mean flow is assumed to vary only in the body-normal direction. This assumption is valid for small boundary layer growth over a wavelength of the instability wave. Depending on the type of flow and instability, nonparallel terms can have significant influence on the disturbance growth rate [20].

The governing PDEs for the Tollmien-Schlichting and inviscid type (1st and 2^{nd}mode) disturbances are elliptic, so their solution cannot be obtained by simple marching methods. However, for boundary layer flows the equation set is only weakly elliptic along the dominant flow direction. Therefore, with appropriate simplifications, the stability equations can be "parabolized". From a physical view point, the streamwise ellipticity arises from the upstream propagation of acoustic waves and the streamwise viscous diffusion. To render the stability equations parabolic, one must devise a way to suppress this upstream propagation. Herbert [21] proposed a technique which decomposes the disturbance into a rapidly varying

wave-like part and a slowly growing shape function. The ellipticity is retained for the wave part while the parabolization is applied to the shape function. The resulting PSE can be solved by marching along the streamwise direction.

Unlike the Tollmien-Schlichting type disturbances, the governing PDEs for the Goertler problem are naturally parabolic and thus the solution can be obtained by direct marching given a set of initial conditions. A review of the Goertler instability is given by Saric [22]. Goertler vortices arise due to concave curvature, and convex curvature is known to suppress their growth in incompressible [23] and compressible [24] flows. Goulpie *et al* [25] compared linear theory (with the streamwise position held fixed) with a streamwise marching technique and consistently found that adverse pressure gradients have a destabilizing effect on Goertler waves. Arnal provides a description of Goertler stability curves and notes that the Goertler instability is more difficult to influence or control by blowing or suction and that real gas effects have very little effect on Goertler vortices [11].

The PSE account not only for the streamwise variation of the basic flow, but also for the streamwise growth of linear and nonlinear disturbances. It has been compared to classical Orr-Sommerfeld theory [26] and was found to be more consistent in accounting for curvature effects. Various numerical techniques have been developed to solve the linear and nonlinear PSE for two-dimensional compressible boundary layers [27]. A comprehensive analysis of the PSE approach is given by Herbert [12].

Johnson [20] used LST and PSE to investigate the effects of freestream total enthalpy and chemical composition on transition location on sharp cones in a reacting mean flow. He found that transition Reynolds number increased with total enthalpy, and the increase was greater for gases with lower dissociation energies . It was suggested that part of the energy of disturbance fluctuations is absorbed by the chemical components and causes dissociation instead of causing transition. The presence of chemical reactions was demonstrated to have a large effect on disturbance amplification rates, revealing different trends for endothermic and exothermic reactions.

LST and PSE stability analysis requires a high quality mean flow solution, with sufficiently accurate second derivatives. Full Navier-Stokes solvers can be impractical for design purposes due to their heavy computational cost. Often, the Parabolized Navier-Stokes (PNS)

equations are used, particularly for preliminary design and analysis of many high speed vehicles, since their space-marching solution character is more cost effective than time-marching Navier-Stokes solvers. However, Stanek and Rubin [28] note that PNS base flow solutions are frequently unsuitable for stability analysis due to pressure gradient "corrections" applied within the boundary layer, where the streamwise pressure gradient is split in subsonic regions in order to stabilize the flux calculations. They developed a high-order reduced Navier-Stokes approximation for the purpose of computing accurate base flows for use in transition related stability calculations. Stability was maintained through the use of numerical filtering and excellent agreement was found between the results and full Navier-Stokes simulations.

1.1.2 Quiet Wind Tunnels: BAM6QT

In order to achieve supersonic flow, a wind tunnel must contain (or create) a section of high pressure gas that acts to accelerate the flow to sonic conditions at the throat. Some sort of pressure valve or diaphragm is needed to control the release of this high pressure gas into the tunnel. If this diaphragm is located upstream of the test section, then the turbulence generated from its bursting will travel downstream and the flow will be turbulent. To create quiet flow, the diaphragm must be placed downstream of the test section. This is the basis of a *Ludwieg tube*.

The BAM6QT is designed as a Ludwieg tube (Fig. 1.1). A Ludwieg tube is a long pressurized pipe with a converging-diverging nozzle on one end, from which flow exits into the nozzle, test section, and second throat. A diaphragm is placed downstream of the test section. When the diaphragm bursts, a shock wave passes downstream into a vacuum chamber and an expansion wave travels upstream through the test section into the driver tube. The expansion wave isentropically accelerates the flow, reflecting off the endwall of the driver tube and returning to the contraction inlet. Expansion wave reflections occur for a period of time during which the flow remains quiet. Every time the expansion wave in the driver tube reflects from the entrance to the contraction, the stagnation pressure drops. The length of the driver tube governs the useful flow duration: the longer the tube the longer the useful flow. The useful tube run time also depends on the length of time needed to establish

the flow. This starting time is several times the time needed for a particle to cross the test section.

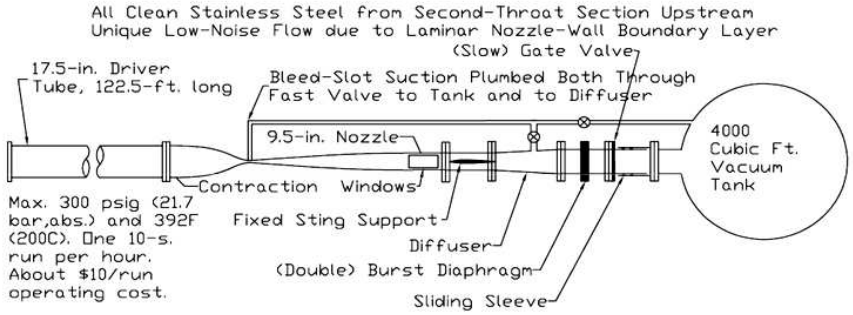

Figure 1.1: Schematic of the Boeing/AFOSR Mach-6 Quiet Tunnel (BAM6QT) [1]

The BAM6QT has been designed to achieve quiet flow for stagnation pressures up to 1034 kPa, corresponding to a unit Reynolds number of $11 \times 10^6\, m^{-1}$ for a stagnation temperature of 433 K at Mach 6. Fig. 1.2 is a typical oscilloscope trace from the BAM6QT that illustrates the substantial difference between noisy and quiet flow. Noise level is defined here as the root-mean-square pitot pressure normalized by the mean pitot pressure. The noise levels[1] in a "quiet" tunnel are generally less than 0.1% [1]. At time $t = 0$ sec the diaphragm bursts and the run begins. Approximately 0.2 sec is required to start up the Mach 6 flow, and quiet flow is only achieved at $t \sim 1.2$ sec. At this point the boundary layer on the nozzle wall switches from turbulent to intermittently turbulent and finally to laminar. The contraction pressure is measured on the right-hand axis and is essentially the stagnation pressure, since the Mach number in the contraction section is less than 0.01. It drops from an initial value of 1100 kPa (160 psia) to 1000 kPa (146 psia) before the flow becomes quiet. Every 0.2 sec the expansion wave returns to the contraction and the stagnation pressure drops roughly 1% as the wave reflects. Five turbulent bursts appear during the course of this run, of approximately 1.5 ms duration each. The run ends after about 7 sec, when the contraction wall pressure has dropped to 724 kPa (105 psia).

Stability analysis was used in designing the BAM6QT nozzle contour in order to delay boundary layer transition and ensure quiet flow [29]. 1st and 2nd mode instabilities, as well

[1]Noise levels are measured as $\frac{\sqrt{\overline{p_p'^2}}}{\overline{p}_p} < 0.0001$, where p_p is pitot pressure.

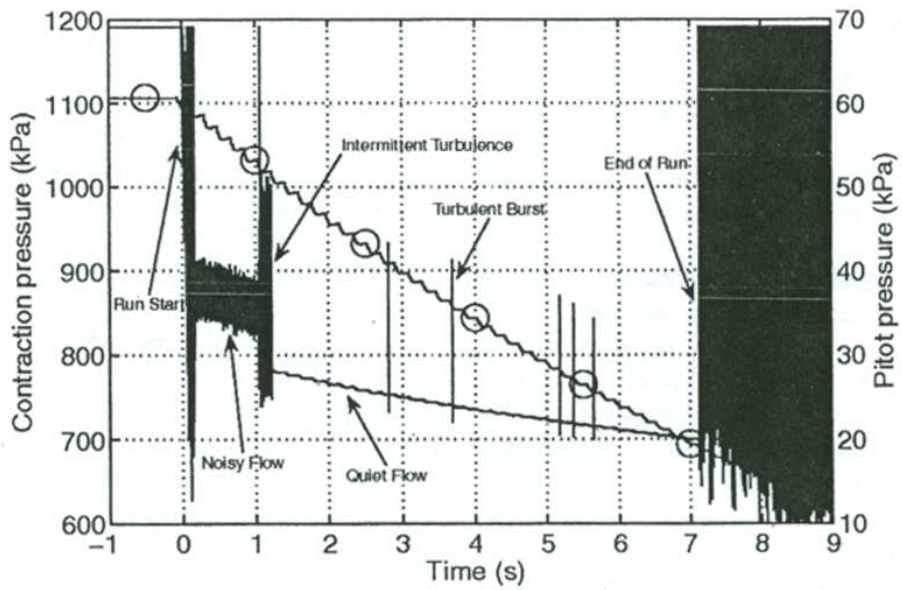

Figure 1.2: Pitot pressure trace showing quiet flow with a few turbulent bursts [1]

as Goertler waves, were studied using LST and the e^N method (section 3.6). Experiments conducted in the BAM6QT reveal how crucial it is to have a quiet flow tunnel for transition research. For example, testing a sharp cone at angle of attack in a *quiet* tunnel was found to have a marked effect on the development of crossflow instabilities [30]. Similarly, experiments conducted on swept wings at NASA Ames' Mach 1.6 quiet tunnel revealed that design practices based on previous results from conventional tunnels were needlessly conservative. Roughness twice as large as previously thought possible could be applied to the attachment line of a swept cylinder before triggering transition [31].

Numerous studies have focused on minimizing the noise radiated from turbulent boundary layers in supersonic wind tunnels [32, 33]. Arnal [11] describes the e^N method in detail and analyzes its advantages and shortcomings. He notes that since this technique is based on linear stability only, receptivity and nonlinear mechanisms are not taken into account. Beckwith *et al* [34] conducted a nozzle optimization study for the quiet Mach 3.5 wind tunnel at NASA Langley using LST and the e^N method. They investigated the effect of nozzle design parameters on the quiet test section length by manipulating the concave curvature and wall angle at the inflection point. Since Goertler vortices appeared to dominate the transition process, the design with a long radial section nozzle yielded a 300% increase in quiet test

region length. A long radial section is significant in that it moves the inflection point far downstream of the throat, which delays the onset of Goertler instability and minimizes the growth rates of the vortices.

1.1.3 Design Methods and Optimization

Numerical optimization techniques have been coupled with CFD in many different applications. The NASA P8 hypersonic inlet was redesigned using an automated numerical optimization procedure that incorporated a 3D RANS code and a gradient-based optimizer [35]. The objective of the redesign was to cancel the cowl shock by modifying the centerbody boundary, and the optimized designs achieved up to 80% improvement. They discovered that the choice of objective function, which is used to drive the optimization, has a significant impact on the final design.

Xu *et al* [36] performed a complete scramjet optimization, including inlet, combustor, and nozzle, using a Bilevel Integrated System Synthesis (BLISS) methodology. BLISS is a way to optimize complex engineering systems using decomposition. The system level optimization, such as the integrated scramjet, which has a relatively small number of design variables, is separated from the numerous subsystem optimizations that may each have a large number of design variables. In this case, the inlet, combustor, and nozzle are each autonomous subsystem optimizations that are conducted concurrently. The system and subsystem optimizations alternate, linked by sensitivity data, producing a design improvement in each iteration.

An airfoil shape was optimized to delay transition by coupling PSE analysis with a gradient-based optimizer [37]. Because delaying transition implies reduction of the viscous drag, this shape optimization essentially designed a wing with optimal viscous drag reduction. While design seems to be the primary area that has been enhanced by linking CFD with numerical optimization, Hogberg [38] employed similar techniques toward a control problem, investigating the optimal control of incompressible boundary layer transition using active control methods such as blowing and suction.

The traditional supersonic nozzle design process involves two separate codes: an inviscid design code and a boundary layer correction code. A quiet nozzle requires additional

stability calculations. First, an inviscid code uses the Method-of-Characteristics (MOC) to determine a suitable inviscid contour and then a boundary layer program computes the laminar boundary layer displacement thickness. Using the boundary layer code to correct the inviscid contour is referred to as the MOC/BL method. The theory used in supersonic nozzle design assumes that the boundary layer thickness is small compared to the characteristic length (*e.g.*, nozzle radius), so the nozzle flowfield can be treated as inviscid for designing the aerodynamic lines. Once the aerodynamic characteristics are determined, a correction is made to account for the displacement thickness of the boundary layer. This basic procedure has been successfully applied to many supersonic and hypersonic nozzles.

While the MOC/BL method has been the conventional design tool used for axisymmetric hypersonic nozzles, it incorrectly assumes that the boundary layer and core flow are not coupled. Figure 1.3 illustrates that each characteristic does not reflect off the inviscid contour at the boundary layer edge but at a point *within* the boundary layer, between the inviscid contour and the wall. Thus, the design characteristic will lag behind the actual characteristic, resulting in incomplete cancellation of expansion waves and deterioration of the flow quality. To solve this problem, the final contour is not obtained by doing a classical boundary layer correction; rather, the inviscid design is used as the starting point for a viscous design optimization based on CFD. An optimization package that utilizes the PNS equations was used to design the shock-free nozzle for the University of Queensland's X3 expansion tube [39], as well as a Mach 7 shock tunnel nozzle [2]. It was noted, however, that this correction to the MOC/BL method is important only for nozzles where the boundary layers grow to a large percentage of the exit radius. This generally occurs for turbulent boundary layers at $M \geq 7$ [2].

Korte [40] modified the MOC/BL design method to account for real gas effects. The imperfect gas effects are treated only in the source flow region (see section 3.1), before the turning region, by computing two separate MOC procedures for the upstream and downstream supersonic sections with different values of gamma. The geometric area ratio is computed using a steady, quasi-one dimensional flowfield solution that includes all real gas effects. Variations of this design procedure have been used to design nozzles at NASA Langley and elsewhere with high quality results [41].

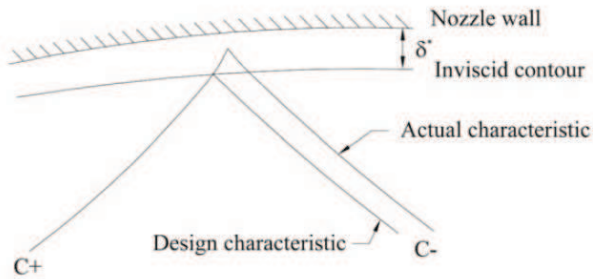

Figure 1.3: Lagging of actual characteristic from MOC/BL design characteristic [2]

Designing a *quiet* nozzle requires not only inviscid design and boundary layer correction, but also additional stability calculations. Designing the quiet nozzles at NASA Langley required a considerable amount of operator intervention, with each computer code running independently and requiring a great deal of data file editing. Furthermore, only one Goertler wavelength could be tested at a time. This laborious process was streamlined in the 1990s when the Mach 4 Ludwieg tube at Purdue University was constructed [42, 43]. The output/input from one code to the next was automated so that the series of codes could be run automatically on a specified nozzle shape, and the stability code was modified to automatically loop through several different frequencies or spanwise wavenumbers in one execution. This alleviated the amount of manual intervention in processing a single nozzle design. However, without being linked to an optimizer, each new design still had to be hand-picked, and it was unclear if it would be an improvement over the previous design.

1.2 Tunnel Startup

Even after an optimal design is found, there is no guarantee that the tunnel will start in the presence of a particular model. The startup problem for supersonic wind tunnels is hardly trivial. Unlike subsonic testing, supersonic tunnel startup does not correlate simply with blockage ratio, due to the differences in the shock/boundary layer interactions generated by different models [44]. There are no standard criteria for supersonic tunnels and engineers have tried various techniques – ranging from tunnel modifications to flow alterations to model adjustments – to achieve tunnel startup in different conditions. During wind tunnel tests for the Voyager entry capsule, for example, a partial unstart of the test section flow

forced engineers to lower the Mach number from Mach 2.2 to Mach 2.0 [45]. In a different experiment, when it was discovered that a diffuser model could not be started in a Mach 3 wind tunnel, the model itself was modified to reduce its blockage ratio, which had the undesirable side-effect of shifting its configuration off the design point [46]. When the blunt Apollo model caused the BAM6QT to unstart, engineers increased the initial stagnation pressure of the tunnel in an attempt to start the tunnel [47]. They also explored the effect of model position on tunnel startup. Seablom *et al* plotted blockage ratio against Mach number for several supersonic tunnels and concluded that tunnel starting is highly dependent on the model geometry and position. Many tunnels also incorporate a bleed section to control boundary layer height and shock/boundary layer interactions, which is often the source of unstart [44]. Wind tunnel models, too, must be designed very carefully, and the desire to make a model as large as possible in order to increase the instrumentation density must be balanced with the need for a small enough model to allow the tunnel to start. Holland *et al* [48] notes that even basic design features of a scramjet inlet, such as contraction ratio and cowl location, must be considered when developing a wind tunnel model, as they can impact the blockage ratio and cause tunnel starting difficulties.

The startup process in a Ludwieg tube, such as the BAM6QT, can be approximated using a one-dimensional method of characteristic analysis [49]. A diaphragm separates high pressure gas in the driver tube from low pressure gas in the vacuum tank region. When this diaphragm bursts, the flow is initiated and an expansion fan propagates upstream. This expansion fan travels through the entire length of the tunnel and eventually reflects off the driver tube endwall. To model this startup process numerically would be extremely expensive, seeing as the driver tube in the BAM6QT is more than 100 feet long and would require a very large computational domain. Furthermore, this transient startup process has little effect on the flowfield once it has reached steady-state. The starting time of a test is defined as the time when steady-state has been reached and the flow properties in the test section become constant. This occurs after the flow has been accelerated by the expansion fan to the point where the nozzle throat chokes. When this happens, a shock is formed just downstream of the throat and slowly travels through the remainder of the nozzle and the test section. A steady flow is established behind this shock, and the start time is therefore

defined as the time when this shock passes out of the test section. Hence, it is only necessary to simulate this shock wave moving through the test section, while the long expansion wave process that precedes it may be ignored.

1.3 Objectives of Research

The objective of this research is to integrate CFD into the design of quiet wind tunnels and the analysis of their performance. The goals are as follows:

Design: A fully automated optimization loop is created, which integrates inviscid contour design, boundary layer growth corrections, full Navier-Stokes analysis and stability calculations to achieve a wind tunnel nozzle with the maximum quiet test section length. The optimization is performed by first creating a response surface and then using a genetic algorithm to sift through the feasible design space.

Analysis: Computations are performed to analyze a proposed expansion for the BAM6QT test section. This modification is designed to enable running larger models with stronger bow shocks, even when the nozzle-wall boundary layer is laminar [50]. CFD is used to determine if such an expansion would cause noise in the quiet test region, and what size model would unstart the tunnel.

Chapter 2

Automated Optimization: Statement of Problem

2.1 Geometry

Each nozzle in the optimization study is modelled after the BAM6QT at Purdue University. The upstream contraction section, including the bleed lip design, matches that of the BAM6QT and blends seamlessly into each new downstream contour (Fig. 2.1). The design Mach number is six, corresponding to an inviscid area ratio of $A_{exit}/A_{throat} = 53.18$. Each inviscid nozzle contour is computed with a default throat radius of 1 inch. The nozzle is then scaled to BAM6QT coordinates by dividing it by 1.622 so that it is consistent with the BAM6QT inviscid throat coordinate[1]. The flow is hypersonic; however, no dissociation or ionization effects have been observed in experiments, so it is treated here as a perfect gas.

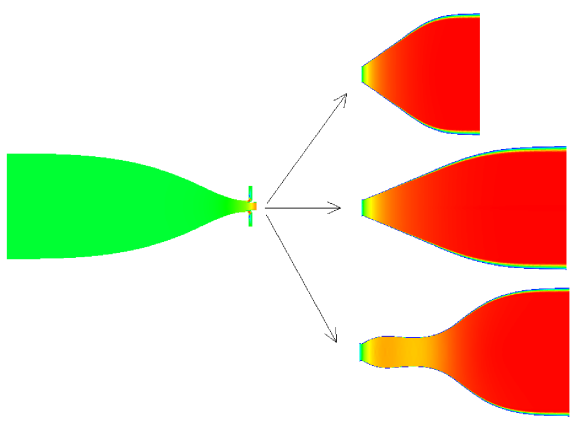

Figure 2.1: Upstream BAM6QT contour with multiple downstream contours

[1]The inviscid BAM6QT throat coordinate is calculated by computing a boundary layer using EDDYBL [51] for the BAM6QT contour and subtracting the displacement thickness. This value compares favorably with the displacement thickness computed from a Navier-Stokes solution of the BAM6QT.

2.2 Stability Objective

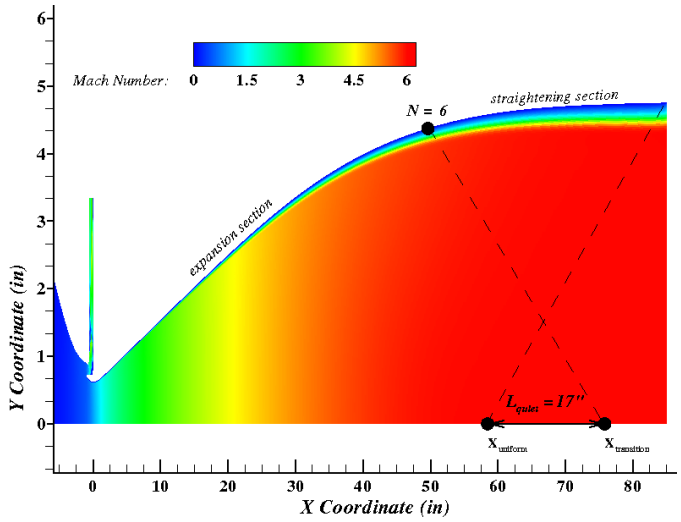

(a) Nozzle that reaches transition

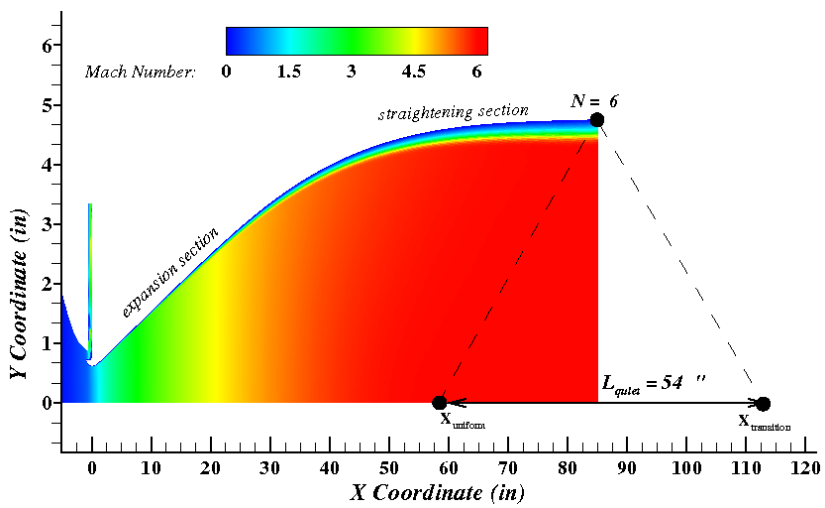

(b) Nozzle that does not reach transition

Figure 2.2: Mach lines indicating the (a) quiet length for a nozzle that reaches transition and (b) maximum quiet length for a nozzle that does not reach $N = 6$ transition

Stability measurements in the NASA Langley Mach 6 tunnel and the BAM6QT reveal that transition occurs at approximately $N = 6$ using the e^N method [52] (see section 3.6). Calculations are performed for two[2] types of instabilities: Goertler and 2nd mode. Goertler

[2]The crossflow instability, which could dominate in 2D nozzles due to corner effects, is neglected here since this investigation focuses on axisymmetric nozzles.

waves develop in regions of concave curvature (denoted as negative curvature). Unfortunately, every wind tunnel must have a region of concave curvature (Fig. 2.2a) which corresponds to the straightening section. This section is crucial for cancelling out the expansion characteristics and producing uniform flow.

Goertler waves are affected by curvature, while 2nd mode waves are affected by boundary layer thickness. For a given design Mach number, the exit-to-throat area ratio is predetermined so a shorter nozzle must have greater curvature to achieve the same exit area. A highly curved nozzle will cause the Goertler instability to grow, but the thin boundary layers associated with a short nozzle will prevent the growth of 2nd mode waves. Presumably, the length that will optimally stabilize one instability will tend to destabilize the other.

However, stability measurements from the BAM6QT [29] and the NASA Langley quiet tunnels [53, 34] indicate that it is the Goertler instability that dominates transition in quiet hypersonic nozzles. For this reason, the transition point throughout the optimization is determined by analyzing only the Goertler instability. 2nd mode stability calculations are performed only on the optimal design to confirm that the 2nd mode does not dominate the Goertler mode.

Each nozzle extends from the throat until the point where it reaches zero-curvature constant area (which becomes the test section). If transition is not yet reached in the nozzle by that point, then, for purposes of comparison and optimization, transition is assumed to occur at the end of the contour. This imposes a limit on the maximum quiet length (Fig. 2.2b). Uniform flow is determined by extending a Mach line from the end of the nozzle in the upstream direction toward the centerline. Transition is determined by extending a Mach line from the transition point at the end of the nozzle in the downstream direction toward the centerline. Since the design Mach number is $M = 6$, the Mach angle is constant:

$$\mu = \sin^{-1}\left(\frac{1}{6}\right) = 9.59^\circ \tag{2.1}$$

Therefore, the maximum quiet length along the centerline is $L_{quiet} = 54$ in. This maximum quiet length is imposed on any nozzle that does not reach $N = 6$ transition.

2.3 Parameterization

Numerous variables affect the stability of a quiet wind tunnel, including shape, temperature distribution, surface roughness, etc. [29]. This investigation focuses on the stability characteristics of different inviscid *shapes*. This is determined in the first step of the design process by the Sivells Design Code [3], which computes the inviscid contour. Three variables are selected as optimization input parameters for Sivells:

RC	=	radius of curvature at the throat, normalized by the throat radius
η	=	expansion angle (in degrees) at the inflection point
bmach	=	centerline Mach number at the intersection of the characteristic that emanates from the inflection point

with the following ranges and discretization:

RC	=	2 - 20; 1
η	=	2° - 10°; 1°
bmach	=	2 - 6; 0.5

These parameters define a unique contour. Fig. 2.3 shows the shape variation as the three parameters are varied for a nozzle with a design Mach number of six. It appears that *RC* (Fig. 2.3c) has little effect on the overall shape of the contour. However, only certain values of *RC* will work with any given combination of η and *bmach* – *e.g.*, a large throat radius of curvature is incompatible with a high expansion angle and high *bmach*. *RC* must therefore be included in the analysis simply to allow the other parameters to vary across their ranges.

2.3.1 Trade Study

Decreasing *bmach* reveals a new class of contours – those with *compound curvature* (Fig. 2.4). Curvature is defined as

$$Curv\ (x) = \frac{f''(x)}{[1 + f'(x)^2]^{\frac{3}{2}}} \tag{2.2}$$

Compound curvature describes a contour with alternating regions of concave and convex curvature. Nozzles with *conventional* contours exhibit an expansion section with positive

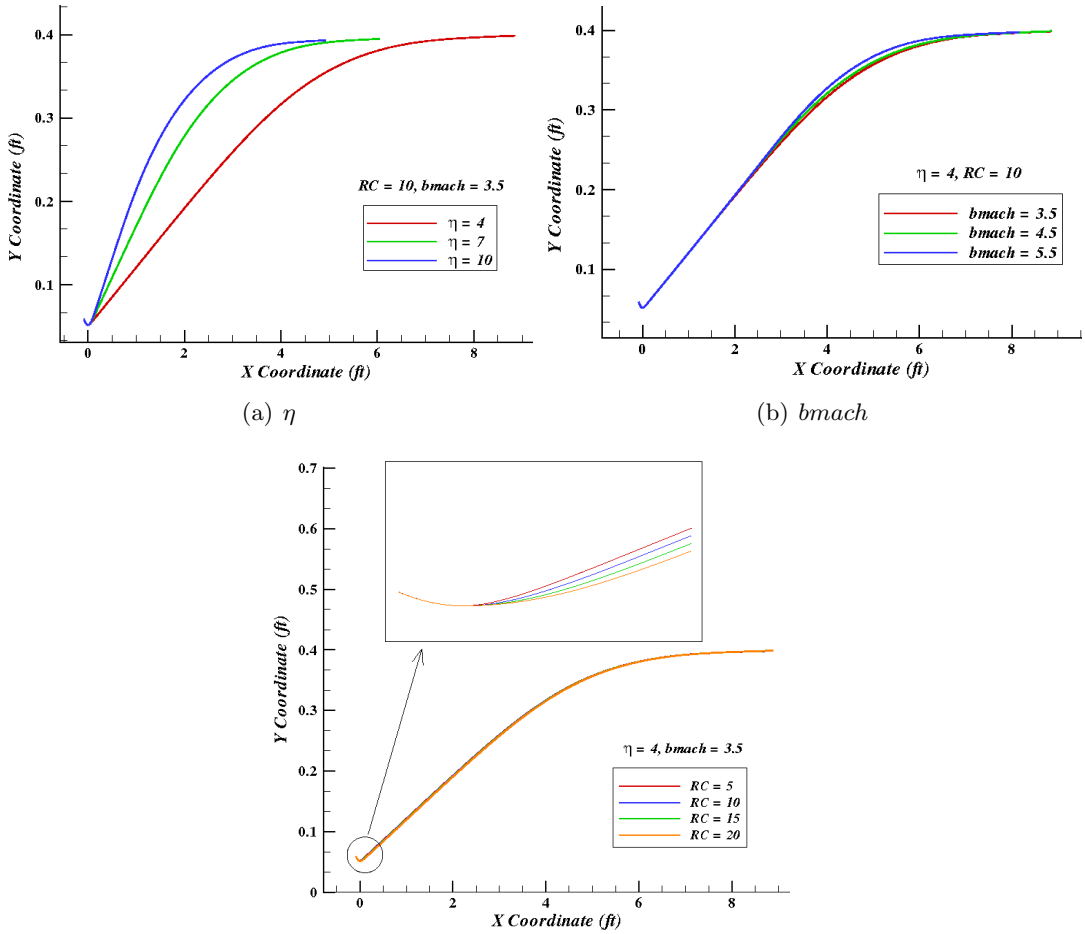

(a) η

(b) *bmach*

(c) *RC*

Figure 2.3: Nozzles with different values of *bmach*, η and *RC*

curvature, followed by a straightening section of negative (unstable) curvature. Nozzles with *compound* curvature have multiple expansion sections. The first straightening section is followed by a second expansion section before a final straightening section achieves uniform flow at the design Mach number (Fig. 2.5). In some cases, the initial "hump" from the first expansion is so large that transition is triggered immediately; however, a gentler compound curvature may have a stabilizing effect, since the initial region of negative curvature is stabilized by the extra section of positive curvature. Indeed, this was also discovered to be the case for incompressible flow [23].

It is clear from this trade study that the *bmach* parameter has a nonlinear effect on the objective of maximuming L_{quiet}. That is, a small variation in *bmach* has a tremendous effect on the curvature – which affects the stability profile of the nozzle. For example, Fig. 2.4

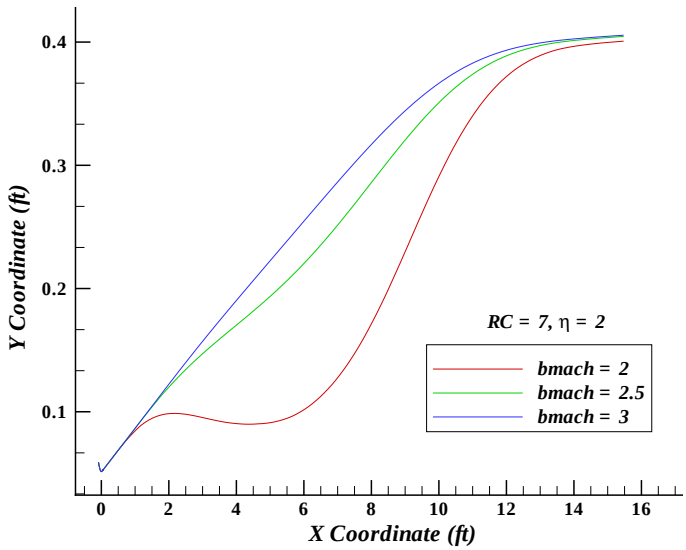

Figure 2.4: Decreasing *bmach* generates nozzles with compound curvature

compares contours with *bmach* varying from 2 to 3. A *bmach* value of 2 yields a highly curved compound nozzle with no quiet length (*i.e.,* the nozzle transitions before uniform flow is reached for Mach 6 flow conditions listed in section 3.5.4), while a *bmach* value of 2.5 yields a nozzle that does not reach transition at all and is assigned the maximum value of $L_{quiet} = 54$ in.

To avoid this nonlinear relationship, a new parameterization is defined based on more logical variables to describe each nozzle shape: **length** and **maximum curvature**. Each set of input variables (RC, η, *bmach*) is used by Sivells to create an inviscid contour. Once created, a contour's total axial length and the maximum value of concave curvature are measured and used to parameterize the design. Thus, the parameters are not known *a priori* – *i.e.,* they are not input variables to the Sivells code. First, the design must be created using the true input variable (RC, η, *bmach*), and only then can the useful optimization parameters (axial length, maximum curvature) be extracted.

In order to accomplish this, a comprehensive table is constructed correlating each ordered set of (RC, η, *bmach*) with a set of (length, curvature) parameters. The optimizer can then choose a (length, curvature) combination, and the corresponding values of Sivells input variables are extracted from the table. This table is created using a simple code that loops through the design space, at increments of 0.1 for η and *bmach* and 0.2 for RC, and calls

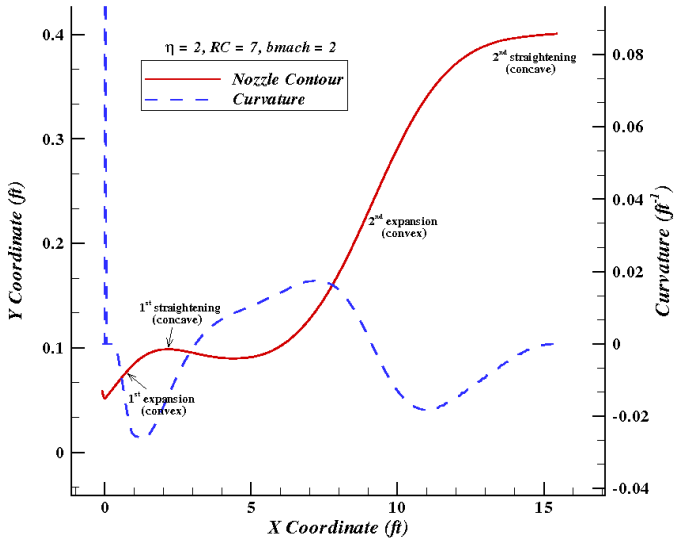

Figure 2.5: Two distinct regions of concave curvature

the Sivells procedure to compute the inviscid contour for each design. It is noted whether a particular design yields a conventional contour, a compound contour, or an error[3].

2.3.2 Design Space

Fig. 2.6 explores the viable design space. A longer nozzle has more gentle curvature, which is expected to delay Goertler-induced transition. Thus, the relationship between length and curvature seems rather straightforward: as length increases, the maximum concave curvature decreases and L_{quiet} will increase. Indeed, Fig. 2.6a shows this to be the case for conventional nozzles. However, compound nozzles seem to etch out a different pattern within the design space (Fig. 2.6b). If only one response surface is created to capture these two different trends, it will likely fail to capture either one. The conventional trend will dilute and smear the compound trend, and vice versa. Therefore, the optimization is divided into two parts, with one response surface for each class of contours.

The goal of this optimization is not simply to maximize the quiet length, but also to minimize the total axial length. From a practical standpoint, a shorter nozzle is more desirable, as it is cheaper to manufacture and requires less space to install. The green

[3]Many combinations of RC, η and $bmach$ will not run in the Sivells code because they are mathematically incompatible. For example, a large throat radius of curvature is incompatible with a high expansion angle and high bmach. The result is an error message from Sivells.

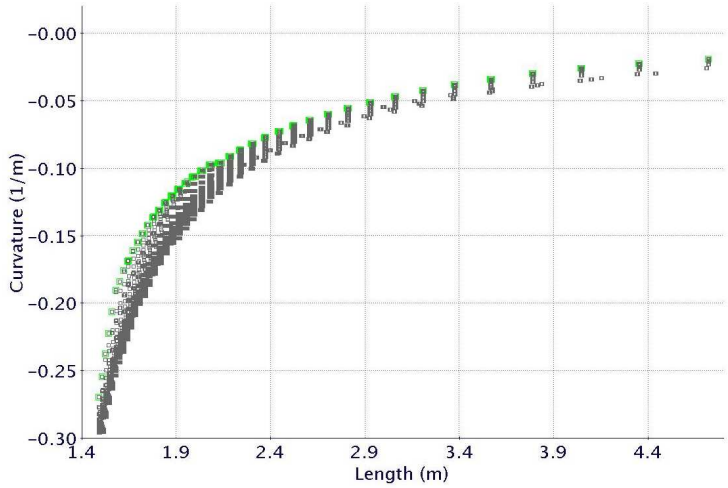

(a) *Conventional*

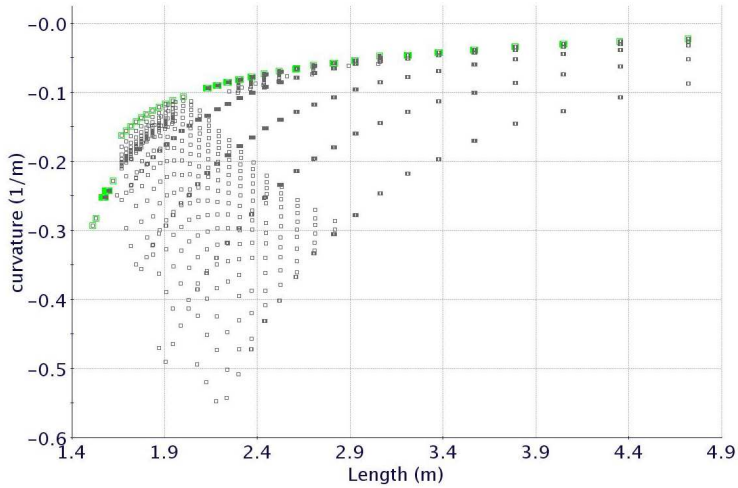

(b) *Compound*

Figure 2.6: Conventional and compound design spaces

highlighted designs in Figs. 2.6a,b indicate the contours with the least amount of concave curvature[4], which is expected to correlate with quiet length. This Pareto front confirms that in order to decrease concave curvature the nozzle must be lengthened. The optimum design will probably lie on one of these curves. For this reason, these designs are examined closely when selecting designs with which to create the response surface.

[4]Since concave curvature is defined as negative curvature, a highly concave nozzle will have a very large negative curvature value. The "maximum curvature" parameter defined here is actually the most negative value. To minimize concave curvature (and achieve a gently curved nozzle) this large negative value must be reduced, so the optimization seeks the most positive values, as close to zero as possible.

Chapter 3

Automated Optimization: Methodology

This study seeks to automate the design optimization of a quiet hypersonic nozzle by linking an optimizer with a flow solver and a stability code within a computerized loop. Fig. 3.1 illustrates the procedure. First, an inviscid contour is designed using the Method of Characteristics (MOC). Second, the compressible boundary layer is calculated and the original contour is corrected for this boundary layer growth. Third, this nozzle shape is supplied to a grid generator and a mesh is created around the new shape. Fourth, the grid is sent to a flow solver which solves for the steady-state solution. Fifth, a stability program uses this flowfield to compute the most unstable disturbance and establish the point of transition along the nozzle contour. This transition point is used to evaluate the objective function. Lastly, the optimizer uses this value to create a response surface which is used to select a new set of parameters for the inviscid contour design.

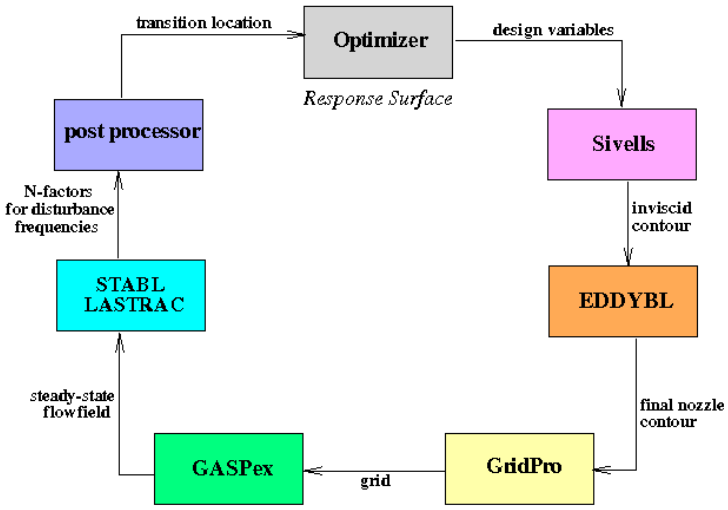

Figure 3.1: Automated Optimization Loop

3.1 Inviscid Contour – Sivells Design Code

Flow expansion in supersonic flow occurs through a system of interacting waves originating from slope changes on the nozzle wall. The upstream, diverging section of the nozzle accelerates the flow and the downstream section uses wave cancellation to straighten the flow. An inflection point separates these two regions. In a conventional "noisy" nozzle, the shape of the upstream expansion contour up to the inflection point is somewhat arbitrary so long as the remaining part of the nozzle can correctly cancel the expansion waves. However in a *quiet* tunnel, this contour must be carefully designed to minimize the growth of Goertler vortices (section 3.6.3). The state-of-the-art in supersonic wind tunnel design involves the use of a 2D or axisymmetric MOC code for determining the inviscid nozzle shapes that produce uniform exit flow. The program used here is the Sivells Design Code [3], which was used in the design of the BAM6QT [29].

Fig. 3.2 is a schematic of the different flow regimes computed by Sivells. Computations generally begin at the throat using a transonic perturbation scheme to compute the flow near the throat, assuming the flow is nearly parallel there. Thus, the upstream subsonic flow must deliver a nearly parallel flow to the throat. These transonic perturbation schemes are only valid for Mach numbers very near one and require some input regarding the shape of the nozzle near the throat, such as the throat radius of curvature. In this study, the BAM6QT coordinates are used for the contraction section *upstream* of the throat, and the throat radius of curvature specified in the Sivells input is the *downstream* curvature, which is seamlessly stitched to the upstream contraction section.

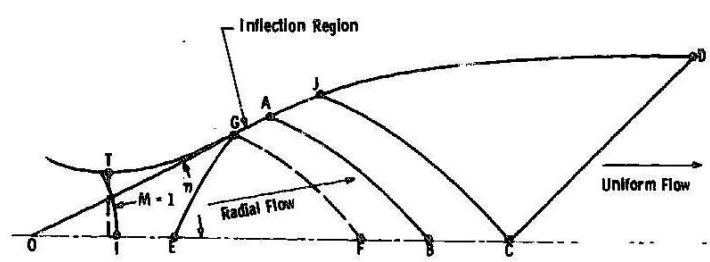

Figure 3.2: Radial flow and expansion regions of inviscid contour [3]

Aside from the input required for this transonic calculation, the nozzle design also requires the Mach number along the nozzle centerline for some distance (until the downstream parallel

flow requirement takes over). Sivells determines the appropriate centerline Mach number distribution that produces a nozzle wall with continuous slope and curvature from the throat to the exit. The centerline Mach number distribution is based on polynomial functions that match the flowfield solutions at each flow region boundary. Once this distribution has been specified, a MOC procedure is used in an inverse design mode to determine an inviscid nozzle wall contour that produces the desired uniform exit flow. This inviscid contour can then be scaled to any size, based on a specified throat radius or exit radius.

Sivells is capable of generating nozzles with a region of *radial flow* between the initial expansion region and the inflection point, *i.e.*, the point at which the wall is shaped to turn the initial characteristics so as to produce uniform exit flow. Section 3.6.3 describes how this helps dampen Goertler waves.

Appendix A contains a sample input file for Sivells. The input parameters are described in section 2.3: RC, η and *bmach*. RC is the ratio of the throat radius of curvature to the throat radius. The throat radius in Sivells is always 1 in. η is the expansion angle at the inflection points G and A in Fig. 3.2. If the first choice of η results in a nozzle design without a radial flow section, η can be lowered until a reasonable design is obtained. *bmach* is the Mach number at point B in Fig. 3.2 and the design Mach number is the Mach number at point C, which remains constant at $M = 6$.

The Sivells output file includes the x and y coordinates of the inviscid contour, as well as the pressure ratio and Mach number at each point. Sivells also writes out the second derivatives of the wall contour, which are used to calculate the local wall curvature for Goertler computations.

3.2 Boundary Layer Correction – EDDYBL

Once the characteristics are determined, a correction is made to account for the displacement thickness of the boundary layer. The underlying assumption behind this method is that the boundary layer thickness is small compared to the nozzle radius, allowing the nozzle flowfield to be treated as inviscid for designing the characteristics. For quiet nozzle investigations, the boundary layers are assumed to be laminar since the boundary layer is only of interest

up to the point where it becomes transitional. The laminar, compressible boundary layer equations are solved using EDDYBL [51]. The inviscid contour output by Sivells is scaled to the BAM6QT throat height (see section 2.1) and the wall pressure is calculated using the pressure ratio from the Sivells output and a stagnation pressure of 150 psi, for which the BAM6QT was designed. The adiabatic wall temperature is $540°R$ (300 K), consistent with the nozzle wall boundary conditions from section 3.5.4[1]. The curvature information from Sivells is written to an EDDYBL input file. Appendix B contains a sample EDDYBL input file.

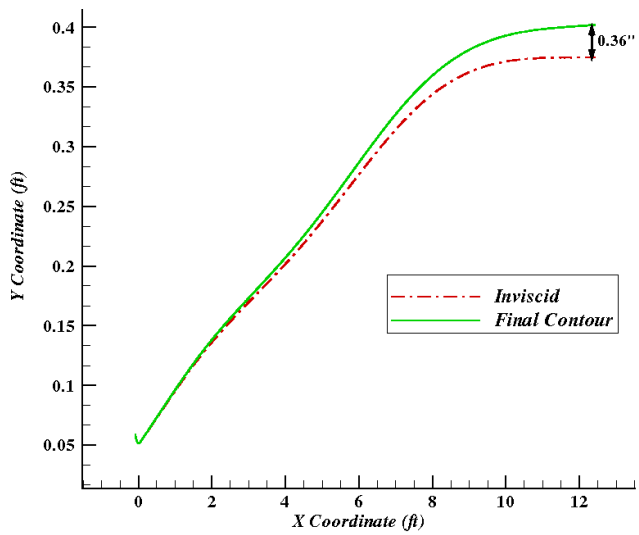

Figure 3.3: Boundary layer correction

The EDDYBL input files for the downstream inviscid contour are appended to the upstream contraction section of the BAM6QT. The boundary layer is calculated starting from the stagnation point on the bleed lip, approximately 1 inch upstream of the throat. The displacement thickness is extracted from the output file and added to the original Sivells contour (Fig. 3.3). The displacement thickness at the end of the nozzle is approximately 0.3 in for most designs.

[1]The wall of the BAM6QT contraction section is heated to $779°R$ (433 K), which corresponds to the inflow conditions in Table 3.1. The nozzle wall is not heated. Once the tunnel is pressurized, the air is left to settle, and the nozzle wall reaches room temperature.

3.3 Mesh Generation – GridPro

The commercial software GridPro [54] is used to generate the structured grid. GridPro is a general purpose elliptic mesh generator that creates a three dimensional, multi-block structured grid. The user input for Gridpro are the surface geometry and the block topology. It is important to note that the same topology definition is used during the optimization while the surface definition changes.

The computational domain has a nonuniform Cartesian mesh (Fig. 3.4) consisting of eight zones. There are approximately $301,000$ cells in total with the following dimensions:

Zone 1	86	$\times$	1025
Zone 2	81	$\times$	1273
Zone 3	777	$\times$	86
Zone 4	257	$\times$	17
Zone 5	49	$\times$	537
Zone 6	769	$\times$	17
Zone 7	17	$\times$	33
Zone 8	113	$\times$	33

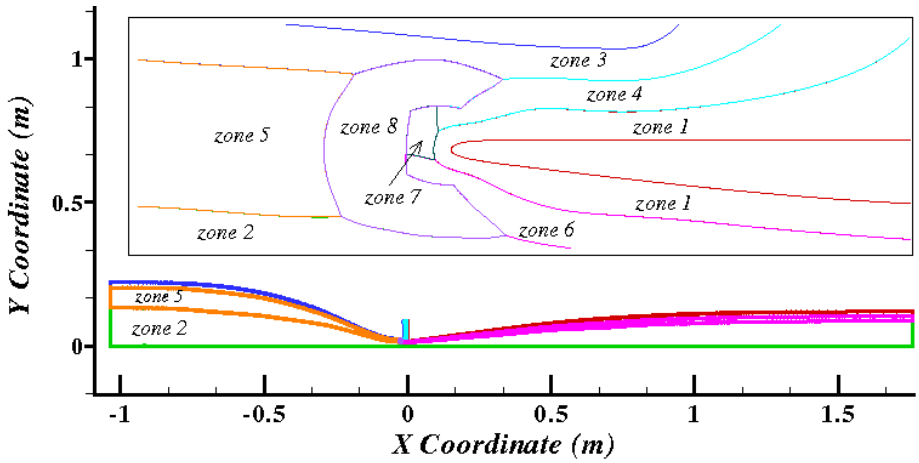

Figure 3.4: Structured grid

Geometric clustering is used near the wall to resolve the boundary layers with a first cell height of 10^{-4} mm and a stretching ratio of 1.1. The boundary layer contains approximately 75 points.

3.4 Flow Solver – GASPex

The flow solver used for these computations is GASPex (General Aerodynamic Simulation Program) [55], a structured multi-block CFD solver that applies to compressible flowfields at approximately Mach 0.2 or higher. It has been extensively validated for a wide variety of hypersonic flows against exact and experimental solutions [19, 56]. The two-dimensional axisymmetric Navier-Stokes equations are solved using a finite volume spatial discretization. The optimization simulations use the steady-state formulation, and the test section expansion calculations (Section 5) use the time-dependent equations. The computations are second order accurate in both time and space.

3.5 Navier-Stokes Equations

The governing equations for unsteady, compressible, laminar, viscous flow of a perfect gas in two dimensions are solved. For an axisymmetric coordinate system, these can be written in conservative form

$$\frac{\partial \mathbf{Q}}{\partial t} + \frac{\partial(\mathbf{F}-\mathbf{F_v})}{\partial x} + \frac{1}{r}\frac{\partial(\mathbf{G}-\mathbf{G_v})}{\partial r} = \frac{1}{r}(\mathbf{S}+\mathbf{S_v}) \tag{3.1}$$

where $\mathbf{Q}(x,t)$ is the vector of conservative variables

$$\mathbf{Q} = \begin{Bmatrix} Q_1 \\ Q_2 \\ Q_3 \\ Q_4 \end{Bmatrix} = \begin{Bmatrix} \rho \\ \rho u \\ \rho v \\ \rho e \end{Bmatrix} \tag{3.2}$$

The inviscid fluxes, $\mathbf{F}$ and $\mathbf{G}$, and the viscous flux vectors, $\mathbf{F_v}$ and $\mathbf{G_v}$, and source terms, $\mathbf{S}$ and $\mathbf{S_v}$, are

$$\mathbf{F} = \begin{Bmatrix} \rho u \\ \rho u^2 + p \\ \rho u v \\ \rho u H \end{Bmatrix}, \qquad \mathbf{G} = \begin{Bmatrix} r\rho v \\ r\rho u v \\ r\rho v^2 + rp \\ r\rho v H \end{Bmatrix} \tag{3.3}$$

$$\mathbf{F}_v = \begin{Bmatrix} 0 \\ \tau_{xx} \\ \tau_{rx} \\ u\tau_{xx} + v\tau_{rx} + k\frac{\partial T}{\partial x} \end{Bmatrix}, \qquad \mathbf{G}_v = \begin{Bmatrix} 0 \\ r\tau_{rx} \\ r\tau_{rr} \\ ru\tau_{rx} + rv\tau_{rr} + rk\frac{\partial T}{\partial r} \end{Bmatrix} \tag{3.4}$$

$$\mathbf{S} = \begin{Bmatrix} 0 \\ 0 \\ p \\ 0 \end{Bmatrix}, \qquad \mathbf{S}_v = \frac{1}{Re}\begin{Bmatrix} 0 \\ 0 \\ \tau_{\theta\theta} \\ 0 \end{Bmatrix} \tag{3.5}$$

$$H = \rho e + p, \qquad \tau_{xx} = 2\mu\frac{\partial u}{\partial x}, \qquad \tau_{rr} = 2\mu\frac{\partial v}{\partial r}$$
$$\tau_{\theta\theta} = -2\mu\frac{v}{r}, \qquad \tau_{rx} = \mu\left(\frac{\partial u}{\partial r} + \frac{\partial v}{\partial x}\right) \tag{3.6}$$

where x and r denote the axial and radial coordinates; ρ, p, e, T, and H denote the density, pressure, energy temperature, and enthalpy; u and v denote the velocities in the x and r directions; μ and k are the viscosity and thermal conductivity of the fluid, respectively. Viscosity of a gas is given by Sutherland's Viscosity Law

$$\mu = 1.456 \times 10^{-6}\frac{T^{3/2}}{T+T_{ref}}\ \text{N-sec/m}^2 \tag{3.7}$$

where T_{ref} is 110.3 K for air.

3.5.1 Space Discretization

For the inviscid fluxes, Van Leer's scheme is used in conjunction with the Minmod limiter. Van Leer's scheme employs *flux vector slitting*, where the flux terms are split and discretized directionally according to the sign of the associated propagation speed. Flux vector splitting schemes are efficient to solve, and Van Leer's method is quite robust.

Consider the one–dimensional Euler equations in semi–discrete form

$$\frac{\partial Q_i}{\partial t} + \frac{(F_{i+1/2} - F_{i-1/2})}{\Delta x} = 0 \tag{3.8}$$

The basic idea behind flux vector splitting is to decompose the flux F into two parts,

$$F = F^+ + F^- \tag{3.9}$$

where $\frac{\partial F^+}{\partial Q}$ has non-negative eigenvalues and $\frac{\partial F^-}{\partial Q}$ has non-positive eigenvalues.

The term F^+ corresponds to waves that move from left to right across the cell interface at $i+1/2$ since the eigenvalues of its Jacobian $\frac{\partial F^+}{\partial Q}$ are greater than or equal to zero. Thus it is reasonable to use $Q^l_{i+\frac{1}{2}}$ to evaluate F^+. Similarly, the term F^- represents the contribution to the flux associated with waves moving from right to left across the cell interface. It is reasonable to use $Q^r_{i+\frac{1}{2}}$ to evaluate F^-.

Van Leer developed a flux vector splitting method based on Mach number [57, 58]. The flux vector F can be written as

$$F = \left\{ \begin{array}{c} \rho a M \\ \frac{\rho a^2}{\gamma}(\gamma M^2 + 1) \\ \rho a^3 M[\frac{1}{(\gamma-1)} + \frac{1}{2}M^2] \end{array} \right\} \tag{3.10}$$

The term involving the Mach number[2] is split into two parts, with ρ and a evaluated using Q^l or Q^r as appropriate. For the mass flux, the term involving Mach number is simply M and is split according to

$$M = M^+ + M^- \tag{3.11}$$

The mass flux is taken to be

$$\rho u = \rho_l a_l M^+ + \rho_r a_r M^- \tag{3.12}$$

Van Leer proposed

$$M^+ = \left\{ \begin{array}{ll} 0 & \text{for } M \leq -1 \\ f_1^+ & \text{for } -1 \leq M \leq 1 \\ M & \text{for } M \geq 1 \end{array} \right. \tag{3.13}$$

and

[2]Note that in this definition the Mach number can be positive or negative.

$$M^- = \begin{cases} M & \text{for } M \leq -1 \\ f_1^- & \text{for } -1 \leq M \leq 1 \\ 0 & \text{for } M \geq 1 \end{cases} \tag{3.14}$$

where M is the average Mach number at the interface and may be defined as

$$M = \frac{u_l + u_r}{a_l + a_r} \tag{3.15}$$

This yields

$$\rho u = \begin{cases} \rho_r a_r M & \text{for } M \leq -1 \\ \rho_l a_l f_1^+ + \rho_r a_r f_1^- & \text{for } -1 \leq M \leq 1 \\ \rho_l a_l M & \text{for } M \geq 1 \end{cases} \tag{3.16}$$

For $M < -1$, the eigenvalues are negative implying that all waves are moving to the left. Then, Q_r can be used to compute ρ and a. Similarly for $M > 1$, Q_l is used to compute ρ and a. The f_1^+ and f_1^- functions are chosen to provide continuity of $M^\pm$ and its first derivative with respect to M at $M = \pm 1$. It can be shown that

$$\begin{aligned} f_1^+ &= \frac{1}{4}(M+1)^2 \\ f_1^- &= -\frac{1}{4}(M-1)^2 \end{aligned} \tag{3.17}$$

The complete expressions for $M^\pm$ become

$$M^+ = \begin{cases} 0 & \text{for } M \leq -1 \\ \frac{1}{4}(M+1)^2 & \text{for } -1 \leq M \leq 1 \\ M & \text{for } M \geq 1 \end{cases} \tag{3.18}$$

and

$$M^- = \begin{cases} M & \text{for } M \leq -1 \\ -\frac{1}{4}(M-1)^2 & \text{for } -1 \leq M \leq 1 \\ 0 & \text{for } M \geq 1 \end{cases} \tag{3.19}$$

For the momentum flux, the term involving the Mach number is split according to

$$(\gamma M^2 + 1) = (\gamma M^2 + 1)^+ + (\gamma M^2 + 1)^- \tag{3.20}$$

The momentum flux is taken to be

$$\rho u^2 + p = \gamma^{-1}\rho_l a_l^2(\gamma M^2+1)^+ + \gamma^{-1}\rho_r a_r^2(\gamma M^2+1)^- \tag{3.21}$$

Van Leer proposed

$$(\gamma M^2+1)^+ = \begin{cases} 0 & \text{for } M \le -1 \\ f_2^+ & \text{for } -1 \le M \le 1 \\ \gamma M^2+1 & \text{for } M \ge 1 \end{cases} \tag{3.22}$$

and

$$(\gamma M^2+1)^- = \begin{cases} \gamma M^2+1 & \text{for } M \le -1 \\ f_2^- & \text{for } -1 \le M \le 1 \\ 0 & \text{for } M \ge 1 \end{cases} \tag{3.23}$$

This yields

$$\rho u^2 + p = \begin{cases} \gamma^{-1}\rho_r a_r^2(\gamma M^2+1) & \text{for } M \le -1 \\ \gamma^{-1}\rho_r a_r^2 f_2^- + \gamma^{-1}\rho_l a_l^2 f_2^+ & \text{for } -1 \le M \le 1 \\ \gamma^{-1}\rho_l a_l^2(\gamma M^2+1) & \text{for } M \ge 1 \end{cases} \tag{3.24}$$

Functions f_2^+ and f_2^- are chosen to provide continuity of (γM^2+1) and its first derivative with respect to M at $M = \pm 1$.

$$\begin{aligned} f_2^+ &= \frac{1}{4}(M+1)^2[(\gamma-1)M+2] \\ f_2^- &= -\frac{1}{4}(M-1)^2[(\gamma-1)M-2] \end{aligned} \tag{3.25}$$

Therefore, the complete expressions for $(\gamma M^2+1)^\pm$ are

$$(\gamma M^2+1)^+ = \begin{cases} 0 & \text{for } M \le -1 \\ \frac{1}{4}(M+1)^2[(\gamma-1)M+2] & \text{for } -1 \le M \le 1 \\ \gamma M^2+1 & \text{for } M \ge 1 \end{cases} \tag{3.26}$$

and

$$(\gamma M^2+1)^- = \begin{cases} \gamma M^2+1 & \text{for } M \le -1 \\ -\frac{1}{4}(M-1)^2[(\gamma-1)M-2] & \text{for } -1 \le M \le 1 \\ 0 & \text{for } M \ge 1 \end{cases} \tag{3.27}$$

For the energy flux, the term involving the Mach number is $M[(\gamma-1)^{-1}+\frac{1}{2}M^2]$, and is split as

$$M[(\gamma-1)^{-1}+\frac{1}{2}M^2] = M[(\gamma-1)^{-1}+\frac{1}{2}M^2]^{+} + M[(\gamma-1)^{-1}+\frac{1}{2}M^2]^{-} \tag{3.28}$$

The energy flux is

$$(\rho e+p)u = \rho_l a_l^3 M[(\gamma-1)^{-1}+\frac{1}{2}M^2] + \rho_r a_r^3 M[(\gamma-1)^{-1}] + \frac{1}{2}M^2]^{-} \tag{3.29}$$

Van Leer proposed

$$M[(\gamma-1)^{-1}+\frac{1}{2}M^2]^{+} = \begin{cases} 0 & \text{for } M \le -1 \\ f_3^{+} & \text{for } -1 \le M \le 1 \\ M[(\gamma-1)^{-1}+\frac{1}{2}M^2] & \text{for } M \ge 1 \end{cases} \tag{3.30}$$

and

$$M[(\gamma-1)^{-1}+\frac{1}{2}M^2]^{-} = \begin{cases} M[(\gamma-1)^{-1}+\frac{1}{2}M^2] & \text{for } M \le -1 \\ f_3^{-} & \text{for } -1 \le M \le 1 \\ 0 & \text{for } M \ge 1 \end{cases} \tag{3.31}$$

This yields

$$(\rho e+p)u = \begin{cases} \rho_r a_r^3 M[(\gamma-1)^{-1}+\frac{1}{2}M^2] & \text{for } M \le -1 \\ \rho_l a_l^3 f_3^{+} + \rho_r a_r^3 f_3^{-} & \text{for } -1 \le M \le 1 \\ \rho_l a_l^3 M[(\gamma-1)^{-1}+\frac{1}{2}M^2] & \text{for } M \ge 1 \end{cases} \tag{3.32}$$

The functions f_3^{+} and f_3^{-} are chosen to provide for the continuity of $M[(\gamma-1)^{-1}+\frac{1}{2}M^2]$ and its first derivative with respect to M at $M=\pm 1$.

$$\begin{aligned} f_3^{+} &= \frac{1}{8}(\gamma+1)^{-1}(\gamma-1)^{-1}(M+1)^2[(\gamma-1)M+2]^2 \\ f_3^{-} &= -\frac{1}{8}(\gamma+1)^{-1}(\gamma-1)^{-1}(M-1)^2[(\gamma-1)M-2]^2 \end{aligned} \tag{3.33}$$

The complete expressions for $M[(\gamma-1)^{-1}+\frac{1}{2}M^2]^{\pm}$ become

$$M[(\gamma-1)^{-1}+\frac{1}{2}M^2]^{+} = \begin{cases} 0 & \text{for } M \le -1 \\ \frac{1}{8}(\gamma+1)^{-1}(\gamma-1)^{-1}(M+1)^2[(\gamma-1)M+2]^2 & \text{for } -1 \le M \le 1 \\ M[(\gamma-1)^{-1}+\frac{1}{2}M^2] & \text{for } M \ge 1 \end{cases} \tag{3.34}$$

and

$$M[(\gamma-1)^{-1}+\frac{1}{2}M^2]^- = \begin{cases} M[(\gamma-1)^{-1}+\frac{1}{2}M^2] & \text{for } M \leq -1 \\ -\frac{1}{8}(\gamma+1)^{-1}(\gamma-1)^{-1}(M-1)^2[(\gamma-1)M-2]^2 & \text{for } -1 \leq M \leq 1 \\ 0 & \text{for } M \geq 1 \end{cases} \tag{3.35}$$

3.5.2 Limiter

Van Leer's method is applied in the direction normal to each face of a computational cell. The left and right states, $\mathbf{Q}_l$ and $\mathbf{Q}_r$, are obtained by a third order upwind biased MUSCL reconstruction [59]. A limiter is used to achieve monotonicity of the flow solution, *i.e.*, to eliminate non-physical oscillations around discontinuities, specifically shocks. The Minmod limiter controls oscillations by clipping reconstruction outside the bounds of a cell-face's neighbor.

$$\text{minmod}(x,y) = \begin{cases} x & \text{if} \quad |x| \leq |y| \quad \text{and} \quad xy > 0 \\ y & \text{if} \quad |x| > |y| \quad \text{and} \quad xy > 0 \\ 0 & \text{if} \quad xy < 0 \end{cases} \tag{3.36}$$

The viscous fluxes employ Sutherland's Viscosity Model and are second order accurate. The Prandtl number, which compares the rate of diffusion of momentum with that of heat, is $Pr = 0.72$.

3.5.3 Relaxation to Steady State

Gauss Seidel is an iterative technique that becomes efficient when combined with an inner iteration strategy to improve convergence rate. The Gauss Seidel Relaxation Method [59] is selected as the inner iteration scheme. Five inner cycle iterations are performed until a tolerance of 0.001 is satisfied. Each design runs for $30,000$ iterations at a CFL of 0.8.

3.5.4 Boundary Conditions

The following GASPex boundary conditions are applied to the boundaries:

Inflow

Fixed at Q: Fixed inflow conditions are applied at the boundary as shown in Table 3.1. The inflow boundary parameters correspond to the stagnation conditions:

Table 3.1: Inflow Conditions

p_0	(psi)	150
ρ_0	$(slug/ft^3)$	0.01615
T_0	$(^\circ R)$	779.4
$Mach$		0.0049

Outflow

Forced Outflow: The primitive variables (density, pressure and velocities) are extrapolated from the interior cells for the boundary cells, except that the velocity is forced to exit the boundary.

Bleed Outflow

Riemann/PBack Outflow: A specified backpressure of 1 torr is used for the second ghost cell, along with the internal entropy, total temperature and flow angle. For the first ghost cell values, Riemann variables, internal entropy and the flow angle are used.

Nozzle Wall

No Slip Adiabatic: This is a viscous, solid wall boundary condition where the temperature gradient at the surface is set to zero by extrapolating the pressure. All three velocity components and the pressure gradient are set to zero at the boundary.

$$u = v = w = 0 \tag{3.37}$$

$$\frac{\partial p}{\partial n} = 0 \tag{3.38}$$

$$\frac{\partial T}{\partial n} = 0 \tag{3.39}$$

Contraction Wall

No Slip T=Twall: This is a viscous, solid wall boundary condition where the temperature is set to 433 K, and the no slip conditions (Eq. 3.37) are satisfied.

3.5.5 Centerline

X-Axis Axisymmetric: This is a boundary condition used for axisymmetric-symmetric flows where the singular axis lies along the x axis. The quantities around the x axis are equal except the signs v and w are changed in the ghost cells.

3.5.6 Axisymmetric Side Walls

Positive and Negative Axisymmetric Wall: These are used as side wall boundary conditions in axisymmetric flows.

3.5.7 Initial Conditions

A steady-state solution for a single design was obtained by initializing the flowfield to zero velocity. Once this converged, it was used as the initial condition for all subsequent designs.

3.6 Stability Analysis

The linear parabolized stability equations (PSE) are coupled with the e^N method to predict transition location. Since the PSE constitute an initial boundary value problem, the wavenumber and eigenfunction at the starting location are obtained from linear stability theory (LST).

The stability equations are obtained from the Navier-Stokes equations by first decomposing the instantaneous flow into mean and fluctuating components, $q = \bar{q} + q'$ where q is any flow variable. This decomposition is substituted into the Navier-Stokes equations, and the mean flow equation is subtracted, resulting in the disturbance equation. The disturbance equation can be expressed in the following form for either 2D or axisymmetric flows:

$$\Gamma\frac{\partial\phi}{\partial t}+A\frac{\partial\phi}{\partial x}+B\frac{\partial\phi}{\partial y}+C\frac{\partial\phi}{\partial z}+D\phi+V_{xx}\frac{\partial^2\phi}{\partial x^2}+V_{yy}\frac{\partial^2\phi}{\partial y^2}$$
$$+V_{zz}\frac{\partial^2\phi}{\partial z^2}+V_{xy}\frac{\partial^2\phi}{\partial x\partial y}+V_{xz}\frac{\partial^2\phi}{\partial x\partial z}+V_{yz}\frac{\partial^2\phi}{\partial y\partial z}+F^n=0 \tag{3.40}$$

where $\phi=(\rho_1',\rho_2',\ldots,\rho_{ns}',u',v',w',T',T_v')^T$. The terms in the Jacobian matrices Γ, A, B, $\ldots$,V_{yz} only depend on the meanflow variables and their derivatives, while all of the nonlinear terms are grouped together in F^n.

The disturbance quantities are assumed to be travelling waves of the form

$$\phi=\chi\left(\xi,\eta\right)\exp^{i(\beta z-\omega t)} \tag{3.41}$$

where ξ and η are the body-tangential and body-normal computational coordinates, β is the real spanwise wavenumber, z is the distance in the spanwise direction, and ω is the real frequency. Eq. 3.41 is substituted into Eq. 3.40, and the derivatives are evaluated to yield (in computational coordinates, ξ, η)

$$\tilde{D}\phi+\tilde{A}\frac{\partial\phi}{\partial\xi}+\tilde{B}\frac{\partial\phi}{\partial\eta}+\hat{V}_{\xi\xi}\frac{\partial^2\phi}{\partial\xi^2}+\hat{V}_{\eta\eta}\frac{\partial^2\phi}{\partial\eta^2}+\hat{V}_{\xi\eta}\frac{\partial^2\phi}{\partial\xi\partial\eta}+F^n=0 \tag{3.42}$$

where the Jacobians are given in Reference [20].

χ is decomposed as,

$$\chi=\psi\left(\xi,\eta\right)A\left(\xi\right) \tag{3.43}$$

$$A\left(\xi\right)=\exp^{i\theta(\xi)} \tag{3.44}$$

where $d\theta/d\xi=\alpha\left(\xi\right)$, α is the body-parallel wavenumber in computational coordinates and ψ is the shape function vector. This allows for all of the ellipticity in the wave function to be retained while parabolizing only the shape factor. After further manipulation, the disturbance equation can be expressed as a function of ψ:

$$\hat{D}\psi+\hat{A}\frac{\partial\psi}{\partial\xi}+\hat{B}\frac{\partial\psi}{\partial\eta}+\hat{V}_{\xi\xi}\frac{\partial^2\psi}{\partial\xi^2}+\hat{V}_{\eta\eta}\frac{\partial^2\psi}{\partial\eta^2}+\hat{V}_{\xi\eta}\frac{\partial^2\psi}{\partial\xi\partial\eta}+\hat{F}^n=0 \tag{3.45}$$

For the PSE approximation, the terms $\hat{V}_{\xi\xi}\frac{\partial^2\psi}{\partial\xi^2}$ and $\hat{V}_{\xi\eta}\frac{\partial^2\psi}{\partial\xi\partial\eta}$ are assumed to be small relative to the other terms and can therefore be neglected. Since only small disturbances are considered, their product is small, so the nonlinear terms in $\hat{F}^n$ can similarly be neglected. This generates the *linearized version of the PSE*:

$$\hat{D}\psi + \hat{A}\frac{\partial\psi}{\partial\xi} + \hat{B}\frac{\partial\psi}{\partial\eta} + \hat{V}_{\eta\eta}\frac{\partial^2\psi}{\partial\eta^2} = 0 \tag{3.46}$$

Eq. 3.46 is an initial boundary value problem for the shape function ψ and wavenumber α and can be solved by marching. The marching procedure requires an initial wavenumber solution, which is obtained from linear stability theory (LST). The PSE in Eq. 3.46 can be reduced to the linear stability equations by assuming a quasi-parallel flow such that $\psi = \psi(\eta)$ and $d\alpha/d\xi = 0$. The linear stability equations are

$$\hat{D}\psi + \hat{B}\frac{\partial\psi}{\partial\eta} + \hat{V}_{\eta\eta}\frac{\partial^2\psi}{\partial\eta^2} = 0 \tag{3.47}$$

3.6.1 Transition Prediction using e^N

Since it is not possible to analyze the entire transition process with linear PSE analysis, an approximation is used. Various empirical correlations exist to relate transition onset with boundary layer properties. One such correlation is $Re_\theta/M_e = C$, where Re_θ is the Reynolds number based on boundary layer momentum thickness, M_e is the edge Mach number, and C is an empirical constant in the range of $100 - 500$ [60]. Transition is assumed to occur when the local boundary layer properties satisfy this relation. While many correlations exist [61], no one empirical model can accurately predict transition for a general dataset.

A commonly applied criterion that attempts to predict transition based on the physical mechanism of transition is the e^N method. The value e^N, where N is given by Eq. 3.48, represents the total growth factor of a small amplitude initial disturbance. Presumably, when the disturbance amplitude reaches a critical value the transition process is triggered.

$$N(\omega, \xi) = \int_{\xi_0}^{\xi} \sigma d\xi \tag{3.48}$$

N is the natural log of the total amplitude growth of unstable boundary layer disturbances at a particular frequency ω, ξ is the distance along the surface, ξ_0 is the location of the first

critical point at which the disturbance begins to grow, and σ is the disturbance growth rate defined as

$$\sigma = -Im\left(\alpha\right) + \frac{1}{2E}\frac{dE}{d\xi} \tag{3.49}$$

$$E = \int_n \bar{\rho}\left(|u'|^2 + |v'|^2 + |w'|^2\right) dn \tag{3.50}$$

where $\bar{\rho}$ is the mean flow density, $\left(|u'|^2 + |v'|^2 + |w'|^2\right)$ are the complex fluctuating velocity components, and n is the direction normal to the body surface.

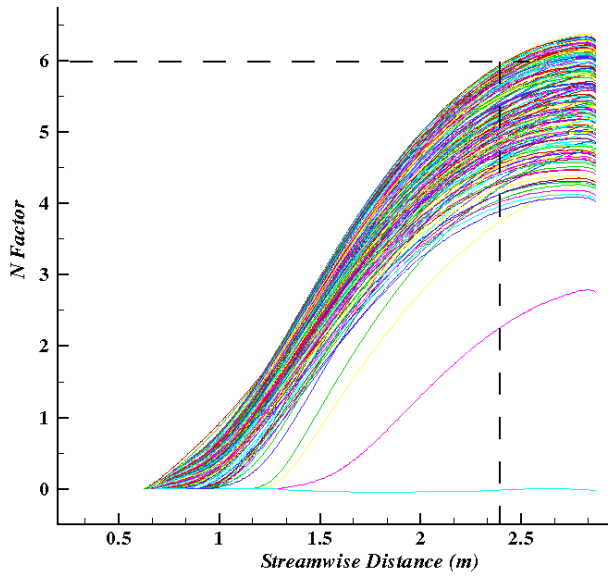

Figure 3.5: N factor output from stability analysis

The value of N that determines transition is highly dependent on the particular geometry and flow conditions of a given problem, and needs to be chosen from comparisons to experimental data. For the Mach 6 quiet wind tunnel calculations in this study, $N = 6$ is used to determine transition (see Section 2.2). Fig. 3.5 is a sample N-factor output from a stability calculation. Each curve represents a separate disturbance (as defined by wavenumber, frequency and initial location). The first curve that reaches $N = 6$ is the most unstable disturbance that causes the flow transition. The streamwise location along the x-axis where this curve intersects with the $N = 6$ line is the transition location along the surface. For the plot in Fig. 3.5, transition occurs around 2.4 m.

3.6.2 1st and 2nd mode – STABL

Mack [15] showed that disturbances with the form given in Eq. 3.41 can have several modes. The first mode is analogous to the Tollmien-Schlichting waves in incompressible flow. It is damped by wall cooling and is most amplified at an oblique angle. The second mode can be considered a trapped acoustical wave. It is amplified by wall cooling and it is most amplified when it is 2D. Higher modes exist, but they always have lower amplification rates than the first or second mode.

The stability code used for these calculations is STABL (Stability and Transition Analysis for Hypersonic Boundary Layers), which was developed by Heath Johnson at University of Minnesota in the late 1990's [20]. STABL was verified and validated in 2005 [60] and compares favorably with experiments [62] and older LST codes, such as e**Malik [63]. STABL has recently been used, with great success, to support transition experiments in the CUBRC LENS I hypervelocity shock tunnel [64].

A sample script to run STABL in batch mode is included in Appendix C. To test for 1st and 2nd mode instabilities, a test matrix of initial location (where the PSE marching and e^N integration begin), frequency ω and spanwise wavenumber β must be specified. STABL's automatic test matrix generator plots the estimated 2D first and second mode frequencies[3]. The first mode disturbance frequencies are estimated based on the boundary layer thickness and edge velocity. Second and higher modes, which represent acoustic waves, are more accurately estimated using the characteristic time of wave travel between the wall and the relative sonic line. Each mode has a range of unstable frequencies at which disturbances will be amplified. The extent of the test matrix is chosen to contain the likely upstream values of the critical disturbance frequencies. An initial strategy for creating test matrix points is to cover the entire 1st and 2nd mode estimate curves. After the initial analysis, if it turns out the 1st mode disturbances dominate, nonzero values of β can be added to test for oblique waves [65]. Figs. 3.6a,b show preliminary tests for a sample design to determine the appropriate range of ω and β. These results are generated by the "automated test matrix generator" in STABL. Fig. 3.6a shows the N-factors with the corresponding envelope of most

[3] 2D waves have a spanwise wave number, β, equal to zero

unstable frequencies. By comparing the trends of the 1st and 2nd mode frequency estimates in Fig. 3.6b with the most unstable frequency at each location (green), it is apparent that while initially 1st mode disturbances are most amplified, 2nd mode disturbances begin to dominate after approximately 0.8 m. This is clear from the green line which roughly follows the blue 1st mode estimate until 0.8 m, and then follows the orange 2nd mode estimate. This seems consistent with Mack's findings regarding sharp cone boundary layers at $M = 6.8$ [66]. When he compared his calculated amplification rates with the experimentally determined rates from Stetson's famous stability experiments [67], he found that although there were a number of differences between them, both revealed that the only significant instability at $M = 6.8$ comes from the second mode 2D waves.

Since the 2nd mode frequencies dominate, it is not necessary to examine the oblique first modes with nonzero β. Furthermore, since 2nd mode 2D waves are more unstable than 2nd mode 3D waves, only 2D waves need to be tested in this investigation. Frequencies that are tested range from $5 - 500\ kHz$ and the initial locations span the length of the contour (which changes for each design).

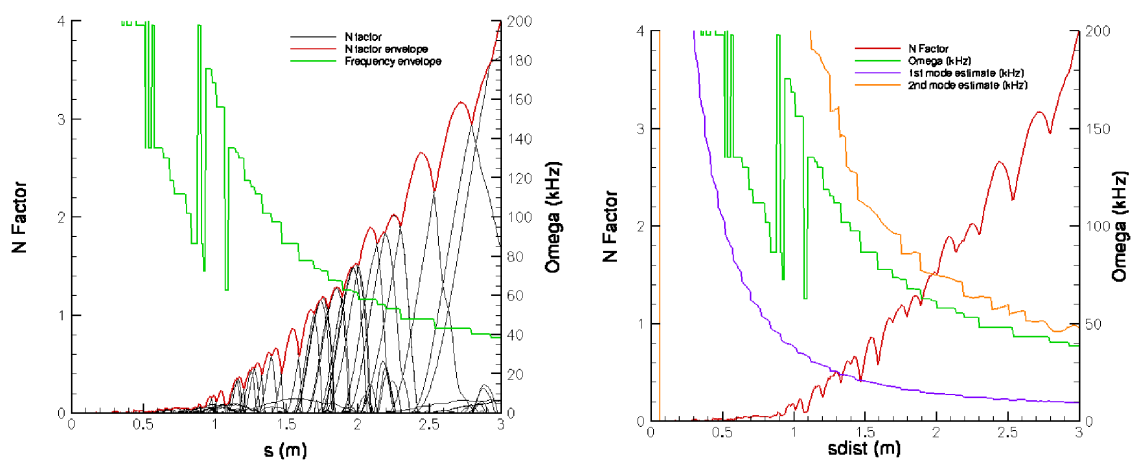

(a) (b)

Figure 3.6: Frequency estimates from STABL indicate that the second mode dominates

Preliminary tests and prior investigations [29, 53] indicate that the 1st and 2nd mode instabilities do not dominate in quiet hypersonic wind tunnels; rather, the Goertler mechanism dominates the transition process. Therefore, STABL is not run as part of the original optimization loop. STABL is used only after a set of optimal solutions are obtained, to

ensure that the 1st and 2nd mode N-factors do indeed fall within the acceptable limit.

3.6.3 Goertler Vortices – LASTRAC

Regions of concave curvature give rise to yet another instability mechanism: Goertler waves. These are stationary, counter-rotating vortices along the streamwise direction that nonlinearly modify the meanflow. Wind tunnel design requires concavity at a minimum of one inflection point in order to cancel the characteristics from the expansion section and achieve uniform flow. One common method of delaying Goertler-induced transition along nozzle walls is to insert a straight wall, radial flow section upstream of the inflection point of the nozzle contour [68, 69]. Thus, the Goertler instability is not initiated until the beginning of the concave nozzle wall, and then a slow expansion is used to achieve the desired Mach number. The slower expansion implies larger radii of curvature that result in smaller overall growth of Goertler vortices.

Goertler stability calculations are carried out using LASTRAC (Langley Stability and Transition Analysis Code) [70]. LASTRAC is a state-of-the-art stability code that can model 1st and 2nd mode, crossflow, and Goertler instabilities using LST as well as linear and nonlinear PSE.

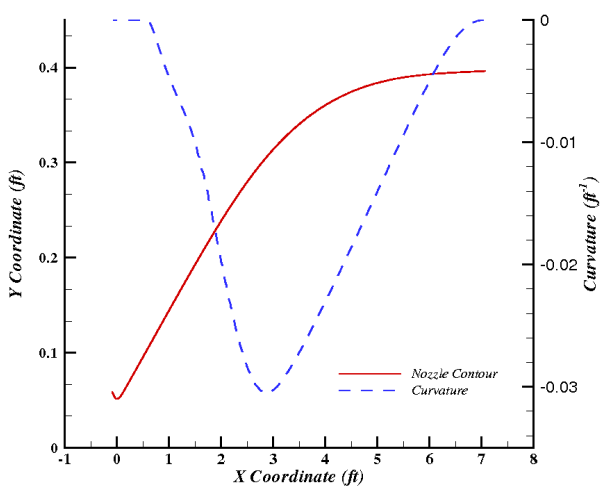

Figure 3.7: Streamwise curvature for each contour is used to determine Goertler growth

A sample LASTRAC input file is included in Appendix D. Goertler waves are steady, so the frequency is set to 10^{-4} Hz (close to zero), but it has a range of unstable β values. The

streamwise curvature at each station must be specified in the meanflow input, and this is taken from the inviscid curvature values output by Sivells (Fig. 3.7). The curvature is set to zero between the bleed lip and the throat (since Sivells does not output that portion of the contour, and the curvature is small in that region anyways). The streamwise curvature determines when a Goertler mode will grow, so a postprocessing code automatically runs through the list of curvatures at each streamwise station until it reaches a concave (negative) curvature of $10^{-4}\ m^{-1}$. Unlike the STABL input file, a separate LASTRAC input file is required for each initial location to be tested. Six locations are tested, beginning with the first station with curvature $\geq 10^{-4}\ m^{-1}$, denoted as station i, and at stations $i+3$, $i+6$, $i+9$, $i+12$ and $i+15$. LASTRAC runs on a single processor, but each of the six input files can be run simultaneously on different CPUs.

In an axisymmetric boundary layer, the use of an integer azimuthal wavenumber, n, is more physical than an arbitrary real spanwise wavenumber β [53], so n is specified instead of β and ranges from 35 to 210. This is equivalent to assuming a fixed number of waves around the nozzle circumference. The corresponding non-dimensional spanwise wavenumber is $\beta = nl/r_b$, where l is the length scale and r_b is the local radius. The length scale is simply the boundary layer similarity length scale defined by $l = \sqrt{\nu_e x/u_e}$, where the subscript e indicates boundary layer edge values.

3.7 Optimization Software – modeFRONTIER

All of the software components are linked within the commercial optimization package modeFRONTIER [71]. modeFRONTIER is a multi-objective optimization and design environment that allows easy coupling to almost any computer aided engineering tool.

3.7.1 Objective Function

The region of useful, quiet flow in a supersonic wind tunnel lies between the characteristics marking the onset of uniform flow, and the characteristics marking the upstream boundary of acoustic radiation from the onset of turbulence in the nozzle wall boundary layer (Fig.

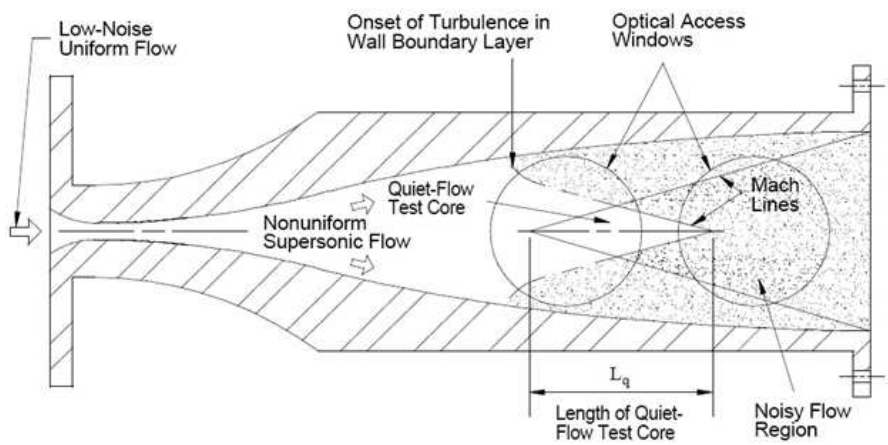

Figure 3.8: Schematic of quiet flow region in a supersonic tunnel [4]

3.8). To maximize the length of this region, the objective function is

$$f := max\left[L_{quiet}\right] \tag{3.51}$$

where L_{quiet} is defined as $X_{transition} - X_{uniform}$, where X is the axial coordinate along the centerline (Fig. 2.2). Sivells outputs the **centerline location** of the onset of uniform flow, $X_{uniform}$. However, the stability codes return the transition **location along the contour**, not the centerline, since sound is radiated downstream along Mach lines from the initial location of transition along the wall. The Mach line is determined by the Mach angle

$$\mu_\infty = \sin^{-1}\left(\frac{1}{M_\infty}\right) = \sin^{-1}\left(\frac{1}{6}\right) = 9.59^\circ \tag{3.52}$$

$X_{transition}$ along the centerline is then calculated from the (x_{tr}, y_{tr}) coordinates of the location of transition along the contour according to the formula

$$X_{transition} = x_{tr} + \frac{y_{tr}}{\tan\mu_\infty} \tag{3.53}$$

3.7.2 Response Surface Creation

Fig. 3.9 is a workflow diagram that illustrates how the various codes are linked in modeFrontier. However, it is not a true optimization loop since there is no optimization algorithm used to select each successive design. This is merely used to create a database to build the response surface. The three Sivells input variables are specified, the length and maximum

curvature are extracted and stored to be used later as input variables for the response surface, and a quiet length, L_{quiet}, is returned. This is a user-specified test matrix, sampling the design space around the points that are expected to provide the Pareto front (from Fig. 2.6).

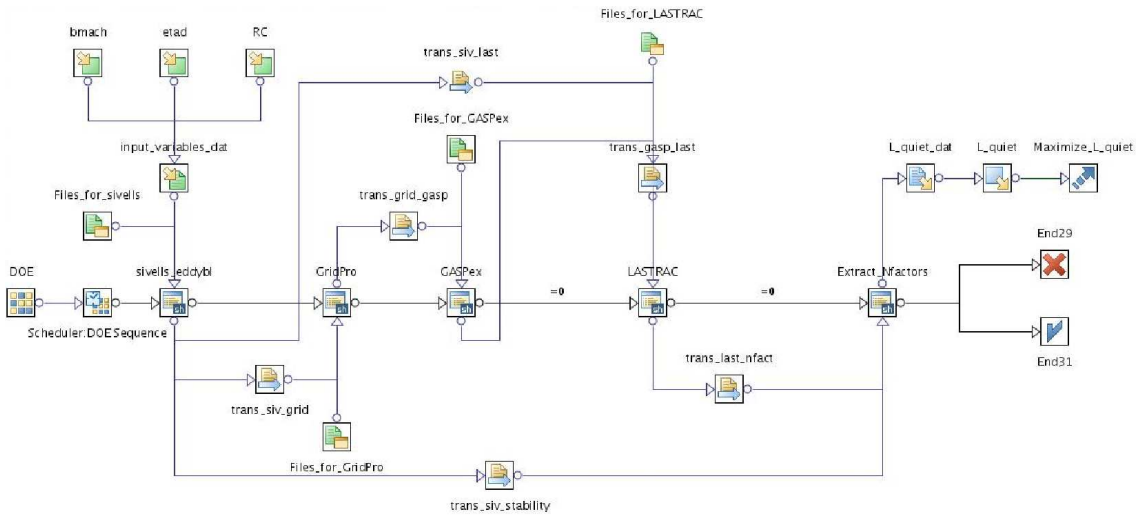

Figure 3.9: Workflow diagram to create the response surface

Once this test matrix is finished running, a database has been created with the following information from each design: axial length, maximum concave curvature, quiet length. A response surface is created from this database where the axial length and maximum curvature are treated as input parameters with the objective to maximize the quiet length. The response surface is a quadratic polynomial created from 20 designs for the conventional contour optimization and from 8 designs for the compound contour optimization. The response surface is written out as a function written in C, which can be run for any set of ($length$, $curvature$) input variables. The function then returns the response surface value of L_{quiet}. Appendix E is the response surface program for the conventional contour optimization.

Table 3.2 lists the response surface properties for both the conventional and compound optimizations. The regression parameter R^2 is calculated as follows :

$$R^2 = 1 - \frac{\sum_{i=1}^{n} (y_i - \tilde{y}_i)^2}{\sum_{i=1}^{n} (y_i - \bar{y}_i)^2} \tag{3.54}$$

Table 3.2: Response Surface Statistics

	CONVENTIONAL	**COMPOUND**
Maximum Absolute Error	11.042	37.058
Average Absolute Error	24.948	16.205
Maximum Relative Error	26.780%	70.519%
Average Relative Error	11.309%	34.022%
Regression	0.95996	0.87632

where y_i is the real value, $\tilde{y}_i$ is the predicted value by the response surface and $\bar{y}_i$ is the mean of all real values. A value very close to one indicates a good synthetic model.

Figs. 3.10a,b are contour plots of the response surfaces. The legends for the response surfaces extend from $L_{quiet} = -200$ in to $L_{quiet} = 1000$ in The reason for these unrealistic values is that this is a purely algebraic model, and the surface does not account for error designs – "holes" in the domain. When the response surface function encounters a steep gradient it will continue down that gradient even if it no longer represents a physical, realistic value. The realistic range is $0'' < L_{quiet} < 54''$. The only relevant segment of the response surface is that portion with L_{quiet} values that lie within this range. The rest of the response surface is filtered out in the next step.

3.7.3 Response Surface Optimization

After the response surfaces are created, a separate optimization is run on each algebraic surface using a genetic algorithm (GA). MOGA II is a second generation multi-objective genetic algorithm included in modeFRONTIER. Genetic algorithms are very robust; however, they require a large number of iterations in order to converge. For this reason, it would be impractical to attempt to run a GA without a response surface, since each iteration with full CFD/stability analysis takes hours to run. However, since the response surface is algebraic, MOGA II runs in under a minute.

Fig. 3.11 shows the workflow diagram for the MOGA II optimization of the response surface. The input parameters at the top are length and maximum curvature and the objectives are to maximize L_{quiet} and to minimize the axial length (which is one of the input parameters). These two objectives are on the right side of the workflow diagram.

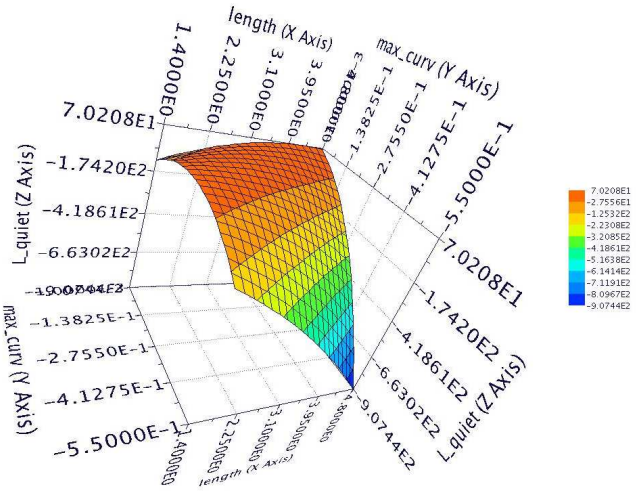

(a) *Conventional*

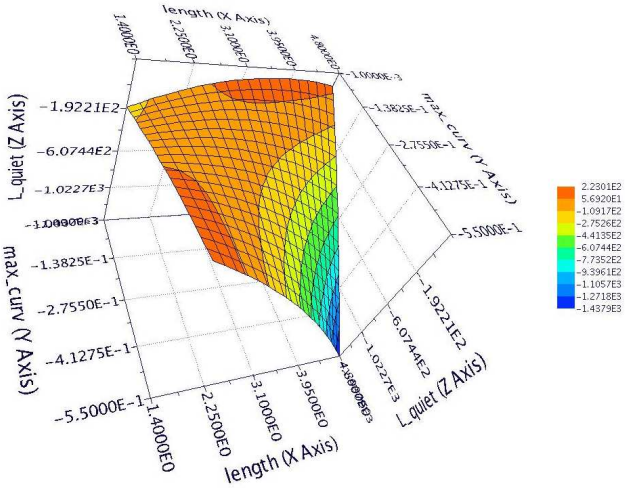

(b) *Compound*

Figure 3.10: Conventional and compound response surfaces

For each design the length and maximum curvature combination is checked against the comprehensive tables (see Section 2.3.1) that correlate the three Sivells variables with length and maximum curvature. If the design is found[4], it is allowed to proceed to the response surface function which calculates L_{quiet}. If the corresponding values are not found, it is assumed that that particular length-maximum curvature combination corresponds to a set of Sivells input parameters that yield an error, and a penalty function is introduced. This function sets L_{quiet} to zero, regardless of the response surface value. Therefore, any infeasible

[4]to within a certain tolerance, since the Sivells input range is discretized to create the table. MOGA II has a much finer discretization of the response surface, so the values never match up exactly.

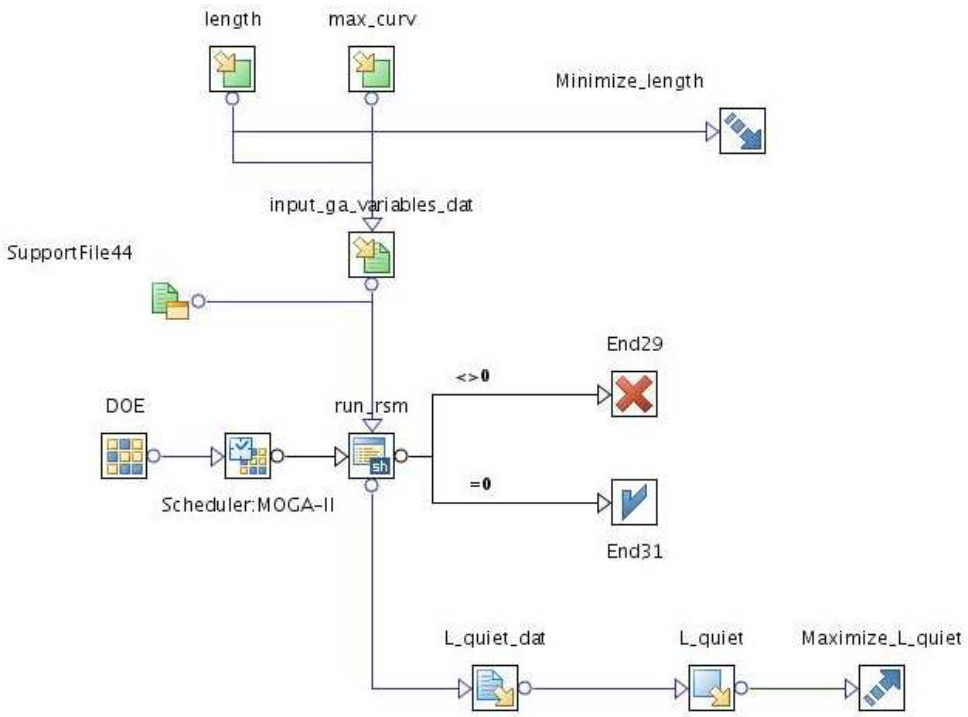

Figure 3.11: Workflow diagram for the response surface optimization

design is assigned a zero quiet length, and will lead the GA to search elsewhere in the design space.

The *run_rsm* script in the middle of the workflow diagram (Fig. 3.11) is the code that 1) searches for error designs, 2) runs a particular design through the response surface code to find the "virtual" output, and 3) imposes a penalty if necessary. The optimal solutions from this optimization are considered "virtual designs" since they are based on the response surface and not on a full CFD/stability analysis. After the optimal virtual designs are found, they are tested with the original Sivells-EDDYBL-GridPro-GASPex-LASTRAC loop in Fig. 3.9 to confirm that the solution is accurate and not merely a consequence of a poor response surface.

3.8 Computing Resources

Computations are performed on a local computer cluster. The Tupolev Linux cluster is part of the Rutgers Center for Computational Design. Tupolev contains 48 processors with 2.4 GHz speed. Each design utilizes 44 CPUs and takes approximately 15 CPU hours to

complete. The majority of each run ($\sim$ 12 hours) is spent converging the flow in GASPex. LASTRAC requires almost three hours and GridPro runs in under an hour.

Chapter 4

Automated Optimization: Results

The results of the GA optimization are displayed in Fig. 4.1. *The only nozzles of interest are those that do not reach transition and are assigned the maximum* L_{quiet} *of* 54 *inches.* The optimal design is then the shortest of these quiet nozzles.

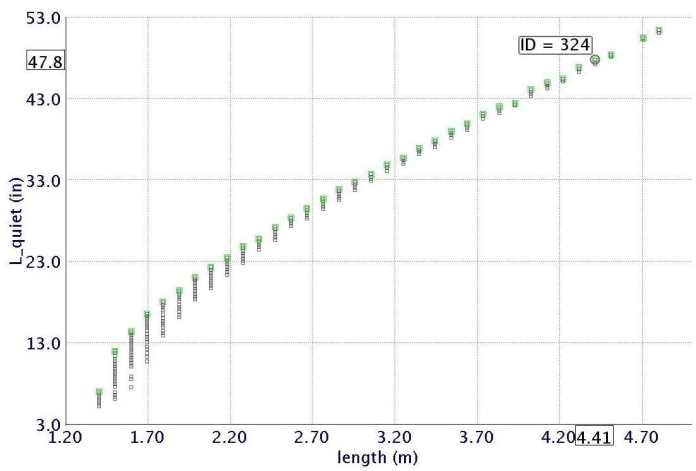

(a) *Conventional*

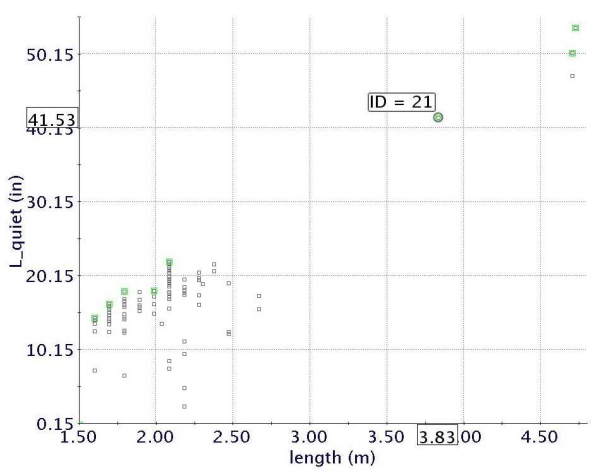

(b) *Compound*

Figure 4.1: Pareto set for conventional and compound contours

Virtual designs from the Pareto front are tested individually using the full CFD/stability analysis that was used to create the response surface. The first design selected from each plot is that in the upper righthand corner of Figs. 4.1a,b. This design corresponds to the longest nozzle with the greatest quiet length. When that design yields a real (not "virtual") maximum L_{quiet} of 54 in, the highlighted green design to its left is tested. Subsequent designs are extracted and tested in this manner, working along the Pareto front from the longest nozzle towards the shortest nozzle, until a design with $L_{quiet} < 54$ in is reached. All points to the left of this design are rejected. The shortest nozzle that meets the $L_{quiet} = 54$ in criterion is the optimal design.

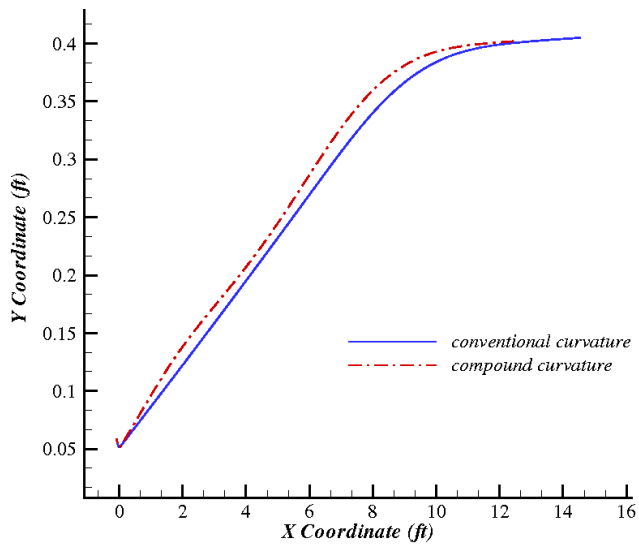

Figure 4.2: Comparison of the two optimal solutions, one from each class of contours

Since the two response surfaces are created with different sets of data, the two optimizations are essentially independent of one another, and each one contains an optimal design. One design has a conventional contour with only one straightening region of concave curvature; the other design has a compound contour with multiple regions of concavity. Both of these contours do not reach a transition value of $N = 6$ within the nozzle, and are therefore assumed to transition at the end of the contour, yielding the maximum quiet length of 54 in. The optimal conventional contour is labeled in green as $ID = 324$ in Fig. 4.1a. The response surface indicates that the quiet length for this design is $L_{quiet} = 47.8$ in with an axial length of 4.41 m. The length and curvature characteristics of this design most closely correspond

to a real design[1] with $RC = 12$, $\eta = 2$, and $bmach = 5.4$. This combination of input values generates a conventional contour with an axial length of 4.438 m and a maximum curvature[2] of $2.965 \times 10^{-2}\ m^{-1}$. This contour is created with Sivells and a full CFD/stability analysis confirms that the quiet length is at least 54 in. The design to the left of $ID = 324$ is also tested with a full CFD/stability analysis and is found to have a quiet length less than 54 in, indicating that the nozzle transitions to turbulence. Thus, $ID = 324$ represents the shortest conventional nozzle that does not reach transition, and it is 4.438 m long.

The same procedure is applied to the compound response surface in Fig. 4.1b. The optimal design is found to be ID = 21, corresponding to a real nozzle with design parameters $RC = 20$, $\eta = 2.6$, and $bmach = 2.6$. This compound nozzle has an axial length of 3.791 m and a maximum curvature of $3.769 \times 10^{-2}\ m^{-1}$. The response surface optimization returns a quiet length of $L_{quiet} = 41.5$ in; however, the complete CFD/stability analysis shows that transition is never reached.

Table 4.1: Comparison of the two optimal solutions

	Conventional	**Compound**
axial length (m)	4.438	3.791
max concave curvature (m^{-1})	2.965×10^{-2}	3.769×10^{-2}
RC	12	20
η	2	5.4
bmach	2.6	2.6

Fig. 4.2 compares the two optimal solutions. The LASTRAC N-factor curves (Fig. 4.3) provide some insight into the benefit of the compound curvature. The "hump" in Fig. 4.3b is a direct result of the slight positive curvature that follows the first concave region. This positive curvature has a stabilizing effect, damping out the growth from the first concave straightening section. This allows for a steeper contour and accounts for the larger maximum curvature value in the compound contour versus the conventional contour (Table 4.1). Steeper curvature in the compound nozzle is responsible for a more rapid expansion

[1] from the comprehensive table that correlates values of RC, η and $bmach$ with axial length and maximum curvature

[2] This is the maximum absolute value, since concave curvature is negative

to the Mach 6 exit diameter, which results in a shorter nozzle. Since the compound contour has a shorter axial length (3.791 m *vs.* 4.438 m) it is the optimal solution. The LASTRAC stability curves indicate that the Goertler waves do not cause boundary layer transition. Further stability analysis with STABL reveals that 1st and 2nd mode waves do not cause transition either. Neither set of N-factors reaches $N = 6$ (Fig. 4.4), and 1st and 2nd mode waves have significantly lower growth rates all along the nozzle. Fig. 4.5 displays Mach number contours for the optimal nozzle design.

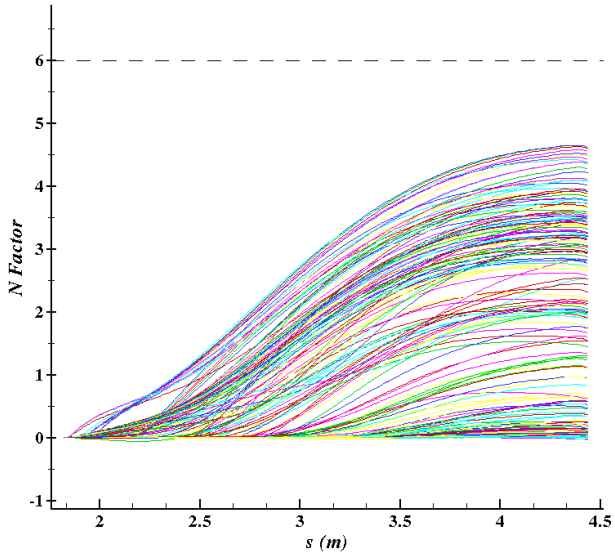

(a) *Conventional*

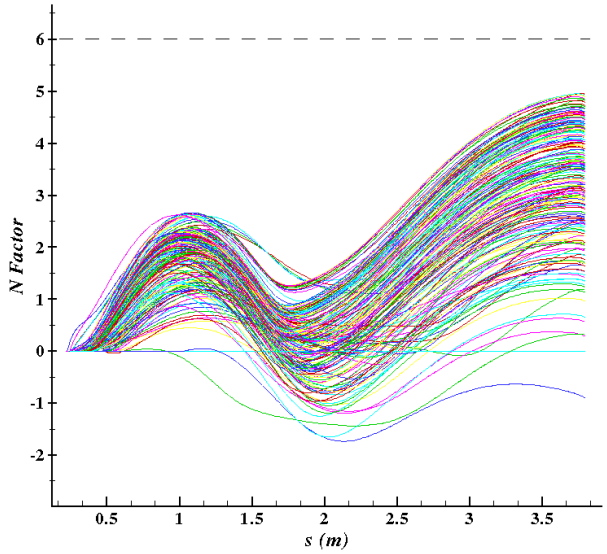

(b) *Compound*

Figure 4.3: LASTRAC N-factor results for the optimal designs

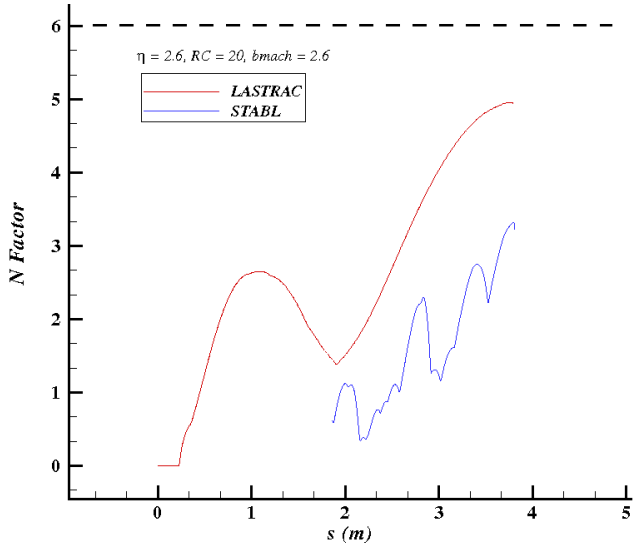

Figure 4.4: STABL and LASTRAC stability envelopes for the optimal design

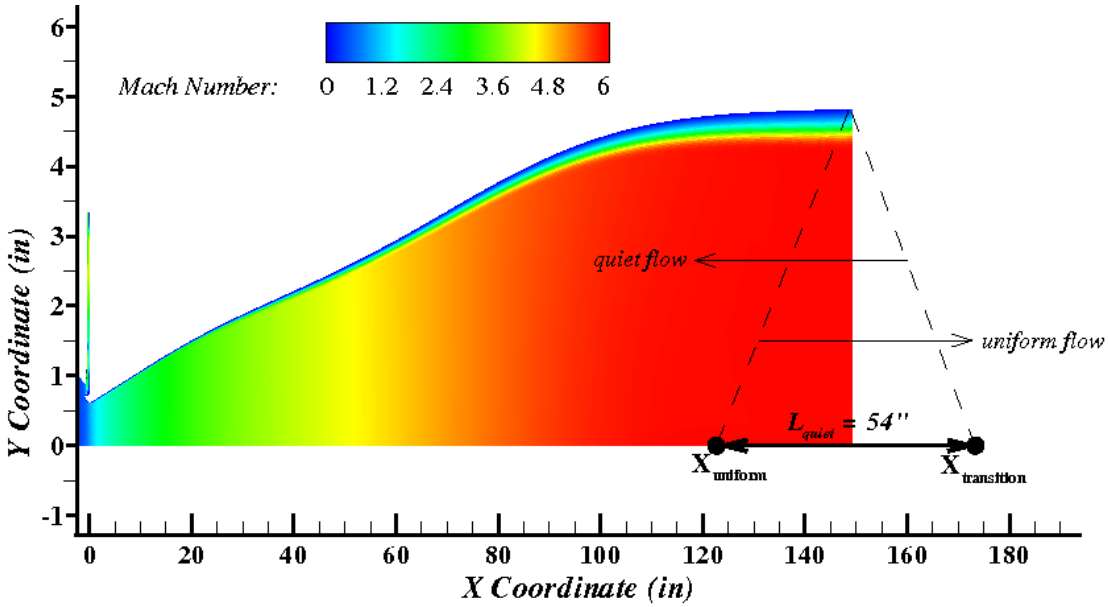

Figure 4.5: Mach contours for the optimal nozzle design

Chapter 5

Test Section Expansion: Statement of Problem

An important concern for the Boeing/AFOSR Mach 6 quiet Tunnel (BAM6QT) is its capability of starting in the presence of a test model. Although slender vehicles are the primary concern in many transition experiments, blunt vehicles are also affected by transition [72] and hence are candidates for testing in the BAM6QT [47]. Shocks emanating from the nose of the test cone and bow shocks from blunter models interact with the boundary layer on the tunnel wall. While disturbances in supersonic flow can only travel downstream, disturbances in the subsonic boundary layer flow in the test section can lead to separated flow upstream in the tunnel nozzle [73]. Laminar boundary layers are more likely to separate than turbulent ones, so shock/boundary layer interactions are more likely to affect upstream flow in a quiet tunnel which has laminar boundary layers at high Reynolds numbers. Laminar shock/boundary-layer interactions are thus a critical issue for determining the largest possible model that can be started in the quiet tunnel.

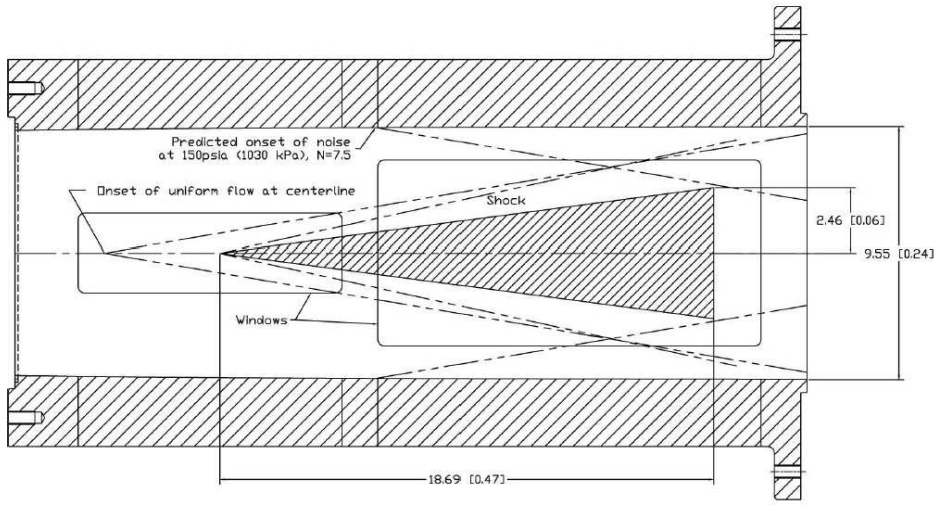

Figure 5.1: Unmodified test section of the BAM6QT with model [1]

The unmodified test section is shown in Fig. 5.1. In this study, computations are performed for an expanded test section of the BAM6QT to determine the effect of the model shock strength on tunnel startup (Fig. 5.2). Separation of the upstream boundary layer is often induced when strong shocks from large and blunt models interact with the nozzle wall boundary layer. The expansion corner of this new section would generate an expansion fan and a shear layer. If the bow shock impinges on the shear layer downstream of the expansion fan, the favorable pressure gradient should inhibit separation from spreading upstream [73]. On the other hand, the shear layer may grow and effectively reduce the useful test cross-section. The purpose of this analysis is to predict what sorts of shocks and shear layers would result from such an expansion, and if this new design would allow larger blunt models to be tested.

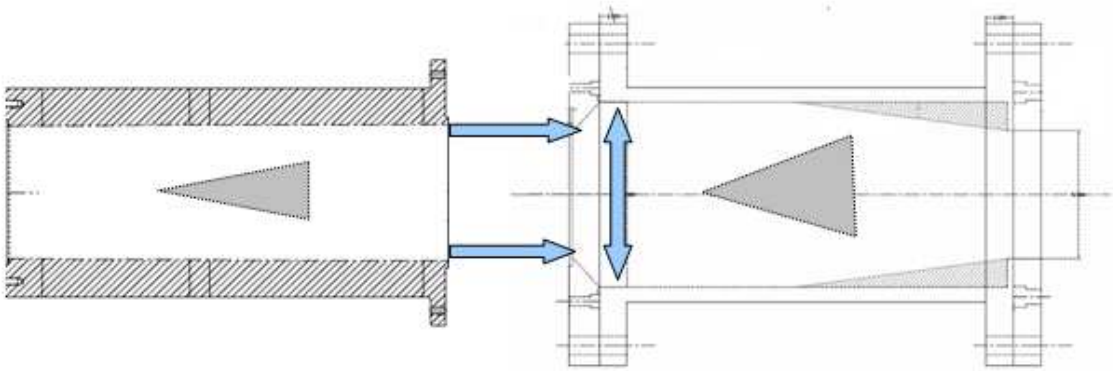

Figure 5.2: Expansion modification of the BAM6QT test section

The selection of an appropriate model to examine the benefits of the test section expansion is a critical issue. Because there are no turbulent boundary layers to contaminate the core flow, quiet tunnels are an ideal setting for transition studies. Such studies are typically performed on sharp and blunt cones at varying angles at attack [67, 61, 18] and therefore a cone at zero angle of attack is selected for this study. A sharp cone is characterized by two parameters: base diameter and cone angle. The base diameter determines the blockage ratio (*i.e.*, ratio of projected model cross-sectional area to tunnel cross-sectional area), while the cone angle affects the strength of the shock wave that forms on the sharp nose of the cone.

5.0.1 Base Diameter

Subsonic tunnel testing has traditionally used the blockage ratio to determine the maximum allowable size for a test model and to correct for blockage effects [74]. Supersonic tunnel testing has also used blockage ratio; however, it is widely recognized that the results on supersonic tunnel starting do not correlate simply with blockage due to the differences in the shock/boundary layer interaction generated by different models [44]. Since there is no universally acceptable criteria for determining the effect of model size on tunnel starting fro supersonic and hypersonic tunnels, a fixed blockage ratio (*i.e.*, fixed diameter) is chosen for simplicity. A 7° half-angle cone with a 5.5-inch base diameter is the largest model that can be started in the unmodified BAM6QT test section at zero angle of attack and stagnation pressure $p_0 = 620\ kPa$ (90 psia) and stagnation temperature $T_0 = 433\ K$ ($779°R$). Therefore, this study investigates cone models with a fixed 5.5-inch base diameter. This corresponds to a blockage ratio of 33.3% for the original, unmodified test section, and 15.9% for the expanded test section.

5.0.2 Cone Angle

Blockage ratio is not the sole criterion that governs the startup process in a supersonic tunnel. If the shock wave generated by the model is strong enough, the interaction of the shock with the boundary layer on the tunnel wall can trigger unstart. The cone angle determines the strength of this shock; the larger the angle, the stronger the shock. This investigation considers several cone sizes at zero angle of attack with a 5.5-inch base diameter with half-angles ranging from 15° to 75°, in order to determine how large a cone could fit in the test section before the tunnel unstarts.

Chapter 6

Test Section Expansion: Methodology

Six axisymmetric cases are run in total: one of the empty section, and five of the section with $15°, 20°, 30°, 50°$ and $75°$ half-angle cones with a 5.5-inch base diameter. The empty section and the $15°$ half-angle cone have a $10°$ compression corner (Fig. 6.1a), but all other computations use a more gradual $1°$ compression[1](Fig. 6.1b).

The structured grids are generated with GridPro [54]. The domain for the empty section consists of one zone with $23,760$ cells (100×241) and the domains for the cone cases consist of four zones and contain approximately $39,000$ points. Grid clustering is performed with a stretching parameter of 1.105 and a first cell height of $10^{-4} ft$, corresponding to $y^+ = 0.1$, along the wall and cone surfaces in order to resolve the boundary layers (Fig. 6.2).

Time-accurate simulations are performed with GASP [55] (see section 3.4). Roe's scheme is used to calculate the inviscid fluxes, along with the Minmod limiter (section 3.5.2) and MUSCL spatial reconstruction.

6.0.3 Space Discretization

Roe's scheme is based on characteristic wave disturbances and captures stationary discontinuities exactly. Roe's method may be derived as follows. The one-dimensional Euler equations in non-conservative differential form [59] are

$$\frac{\partial \mathbf{Q}}{\partial t} + \mathbf{A}\frac{\partial \mathbf{Q}}{\partial x} = 0 \tag{6.1}$$

[1]The compression angle was changed for purely historical reasons. When the computations were started it was expected that the tunnel would be modified with a $10°$ compression ramp, as this requires a shorter section of tunnel to be re-fabricated and installed. Later, this was changed to a $1°$ compression, and subsequent computations were modified accordingly. This variation in geometry should not have a first-order effect on tunnel unstart. In the vicinity of the compression waves near the compression ramp, the flow is mostly supersonic, so the effect of these waves is essentially localized to areas downstream and should not travel upstream and impact the region of interest (the unstart region near the $45°$ expansion).

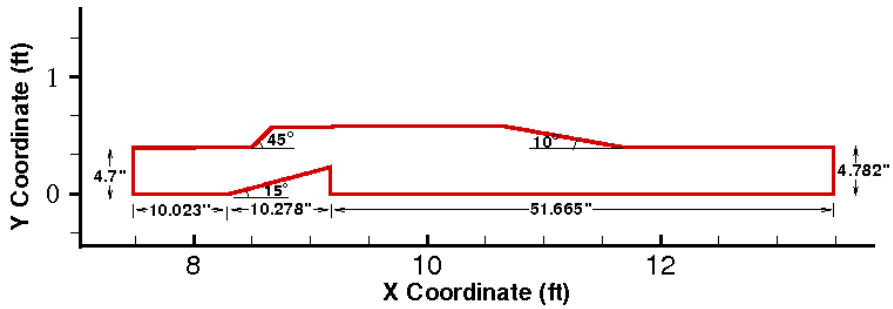

(a) 15° cone

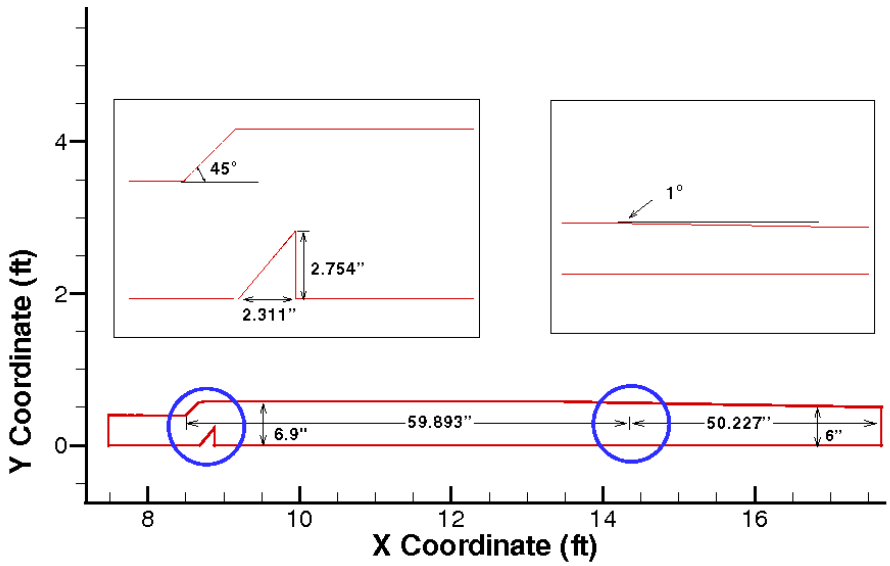

(b) 50° cone

Figure 6.1: Computational domain for (a) 15° and (b) 50° half-angle cones

where $\mathbf{Q}$ is the vector of dependent variables

$$\mathbf{Q} = \left\{ \begin{array}{c} \rho \\ \rho u \\ \rho e \end{array} \right\} \tag{6.2}$$

and $\mathbf{A}$ is the Jacobian matrix defined by

$$\mathbf{A} = \frac{\partial \mathbf{F}}{\partial \mathbf{Q}} = \left\{ \begin{array}{ccc} 0 & 1 & 0 \\ \frac{(\gamma-3)}{2}u^2 & (3-\gamma)u & \gamma - 1 \\ -h_0 u + \frac{(\gamma-1)}{2}u^3 & h_0 - (\gamma-1)u^2 & \gamma u \end{array} \right\} \tag{6.3}$$

where $\mathbf{F}$ is the flux vector and

$$h_0 = e + \frac{p}{\rho} \tag{6.4}$$

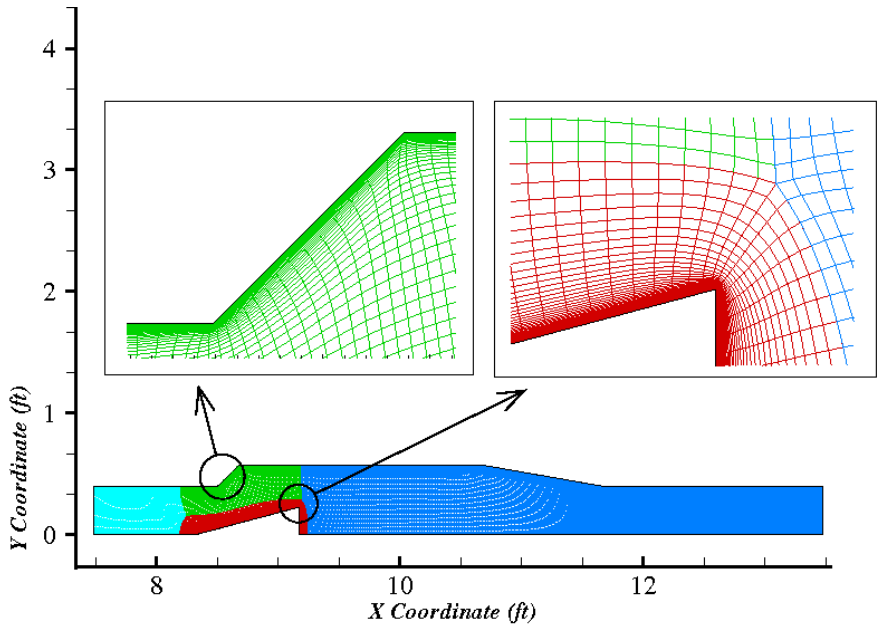

Figure 6.2: Mesh of expanded test section with 15° cone

is the total enthalpy. The general Riemann problem is solved using an approximate form of the Euler equations

$$\frac{\partial \mathbf{Q}}{\partial t} + \tilde{\mathbf{A}}(\mathcal{Q}_l, \mathbf{Q}_r)\frac{\partial \mathbf{Q}}{\partial x} = 0 \tag{6.5}$$

where $\tilde{\mathbf{A}}(\mathbf{Q}_l, \mathbf{Q}_r)$ depends on the left and right states, $\mathbf{Q}_l$ and $\mathbf{Q}_r$, of the general Riemann problem and is assumed constant.

The matrix $\tilde{\mathbf{A}}$ is an approximation of the Jacobian matrix $\mathbf{A}$ and satisfies the following four properties

1. $\tilde{\mathbf{A}}$ provides a linear mapping
2. $\tilde{\mathbf{A}}(\mathbf{Q}_l, \mathbf{Q}_r) \rightarrow \mathbf{A}(\mathbf{Q})$ as $\mathbf{Q}_l \rightarrow \mathbf{Q}_r \rightarrow \mathbf{Q}$
3. For any $\mathbf{Q}_l$ and $\mathbf{Q}_r$, $\tilde{\mathbf{A}}(\mathbf{Q}_l, \mathbf{Q}_r) \times (\mathbf{Q}_l - \mathbf{Q}_r) \equiv \mathbf{F}_l - \mathbf{F}_r$
4. The eigenvectors of $\tilde{\mathbf{A}}(\mathbf{Q}_l, \mathbf{Q}_r)$ are linearly independent

Consider arbitrary piecewise constant functions f and g which have left and right states indicated by f_l, g_l and f_r, g_r, respectively. Identities for these functions are

$$\Delta(f + g) \quad = \quad \Delta f + \Delta g \tag{6.6}$$

$$\Delta(fg) = \bar{f}\Delta g + \Delta f \bar{g} \tag{6.7}$$

$$\Delta \tfrac{1}{\bar{f}} = -\Delta \tfrac{f}{\hat{f}^2} \tag{6.8}$$

where $\Delta f = f_l - f_r$, $\Delta g = g_l - g_r$ and

$$\bar{f} \equiv \tfrac{1}{2}(f_l + f_r) \tag{6.9}$$

$$\hat{f} \equiv \sqrt{f_l f_r} \tag{6.10}$$

The matrix $\tilde{\mathbf{A}}$ can be found as follows. A parameterization vector $\boldsymbol{\nu} = (\nu_1, \nu_2, \nu_3)^T$ is introduced

$$\boldsymbol{\nu} = \left\{ \begin{array}{c} \sqrt{\rho} \\ \sqrt{\rho} u \\ \sqrt{\rho} h_0 \end{array} \right\} \tag{6.11}$$

which yields

$$\mathbf{Q} = \left\{ \begin{array}{c} \nu_1^2 \\ \nu_1 \nu_2 \\ \frac{\nu_1 \nu_3}{\gamma} + \frac{(\gamma-1)\nu_2^2}{2\gamma} \end{array} \right\} \tag{6.12}$$

$$\mathbf{F} = \left\{ \begin{array}{c} \nu_1 \nu_2 \\ \frac{(\gamma-1)\nu_1 \nu_3}{\gamma} + \frac{(\gamma+1)\nu_2^2}{2\gamma} \\ \nu_2 \nu_3 \end{array} \right\} \tag{6.13}$$

Since $\mathbf{Q}$ and $\mathbf{F}$ are quadratic in the elements of $\boldsymbol{\nu}$, it is possible to find matrices $\mathbf{B}$ and $\mathbf{C}$ such that

$$\Delta \mathbf{Q} = \mathbf{B} \Delta \boldsymbol{\nu} \tag{6.14}$$

$$\Delta \mathbf{F} = \mathbf{C} \Delta \boldsymbol{\nu} \tag{6.15}$$

where $\Delta \mathbf{Q} = \mathbf{Q}_l - \mathbf{Q}_r$ and $\Delta \mathbf{F} = \mathbf{F}_l - \mathbf{F}_r$.

Therefore,

$$\Delta \mathbf{F} = \tilde{\mathbf{A}} \Delta \mathbf{Q} \tag{6.16}$$

$$\mathbf{C} \Delta \boldsymbol{\nu} = \tilde{\mathbf{A}} \mathbf{B} \Delta \boldsymbol{\nu} \tag{6.17}$$

$$\Delta \boldsymbol{\nu} = \mathbf{C}^{-1} \tilde{\mathbf{A}} \mathbf{B} \Delta \boldsymbol{\nu} \tag{6.18}$$

and thus, $\tilde{\mathbf{A}} = \mathbf{C}\mathbf{B}^{-1}$

In order to determine the matrix $\tilde{\mathbf{A}}$, $\mathbf{B}$ and $\mathbf{C}$ must be found.

$$\mathbf{B} = \begin{Bmatrix} 2\bar{\nu}_1 & 0 & 0 \\ \bar{\nu}_2 & \bar{\nu}_1 & 0 \\ \frac{\bar{\nu}_3}{\gamma} & \frac{(\gamma-1)}{\gamma}\bar{\nu}_2 & \frac{\bar{\nu}_1}{\gamma} \end{Bmatrix} \tag{6.19}$$

$$\mathbf{C} = \begin{Bmatrix} \bar{\nu}_2 & \bar{\nu}_1 & 0 \\ \frac{(\gamma-1)}{\gamma}\bar{\nu}_3 & \frac{(\gamma+1)}{\gamma}\bar{\nu}_2 & (\gamma-1)\bar{\nu}_1 \\ 0 & \bar{\nu}_3 & \bar{\nu}_2 \end{Bmatrix} \tag{6.20}$$

and thus

$$\tilde{\mathbf{A}} = \begin{Bmatrix} 0 & 1 & 0 \\ \frac{(\gamma-1)}{2}\tilde{u}^2 & (3-\gamma)\tilde{u} & (\gamma-1) \\ -\tilde{h_0}\tilde{u} + \frac{(\gamma-1)}{2}\tilde{u}^3 & \tilde{h_0} - (\gamma-1)\tilde{u}^2 & \gamma\tilde{u} \end{Bmatrix} \tag{6.21}$$

where

$$\tilde{u} \equiv \frac{\bar{\nu}_2}{\bar{\nu}_1} = \frac{\sqrt{\rho_l}u_l + \sqrt{\rho_r}u_r}{\sqrt{\rho_l}+\sqrt{\rho_r}} \tag{6.22}$$

$$\tilde{h_0} \equiv \frac{\bar{\nu}_3}{\bar{\nu}_1} = \frac{\sqrt{\rho_l}h_{0l} + \sqrt{\rho_r}h_{0_r}}{\sqrt{\rho_l}+\sqrt{\rho_r}} \tag{6.23}$$

The quantities $\tilde{u}$ and $\tilde{h_0}$ are the Roe-averaged velocity and the Roe-averaged total enthalpy, respectively. The matrix $\tilde{\mathbf{A}}(\mathbf{Q}_l, \mathbf{Q}_r)$ is the Roe matrix.

The eigenvalues λ_i and the right eigenvectors $\tilde{e}_i$ of $\tilde{\mathbf{A}}$ may be found directly

$$\tilde{\lambda}_1 = \tilde{u}, \qquad \tilde{\lambda}_2 = \tilde{u} + \tilde{a}, \qquad \tilde{\lambda}_3 = \tilde{u} - \tilde{a} \tag{6.24}$$

$$\tilde{e}_1 = \begin{Bmatrix} 1 \\ \tilde{u} \\ \frac{1}{2}\tilde{u}^2 \end{Bmatrix}, \qquad \tilde{e}_2 = \begin{Bmatrix} 1 \\ \tilde{u} + \tilde{a} \\ \tilde{h_0} + \tilde{u}\tilde{a} \end{Bmatrix}, \qquad \tilde{e}_3 = \begin{Bmatrix} 1 \\ \tilde{u} - \tilde{a} \\ \tilde{h_0} - \tilde{u}\tilde{a} \end{Bmatrix} \tag{6.25}$$

where $\tilde{a}$ is the sound of speed based on the Roe-averaged total enthalpy and velocity is given by

$$\tilde{a} = \sqrt{(\gamma-1)(\tilde{h_0} - \tfrac{1}{2}\tilde{u}^2)} \tag{6.26}$$

Table 6.1: Boundary Conditions

	Empty Section	**Section with Cone**
Inflow	pointwise data	pointwise data
	Boundary layer profile: Eddybl Meanflow: $T_0 = 433$ K $P_0 = 620$ kPa [90 psia] $M = 6.1$ $Re = 6.27 \times 10^6\ m^{-1}$	Boundary layer profile: Eddybl Meanflow: $T_0 = 433$ K $P_0 = 620$ kPa [90 psia] $M = 6.1$ $Re = 6.27 \times 10^6\ m^{-1}$
Outflow	forced outflow	forced outflow
Top	no slip, isothermal 300 K	no slip, adiabatic
Centerline	symmetry plane	symmetry plane
Cone Surface	—	no slip, adiabatic

6.0.4 Time Integration

The unsteady solutions are obtained using an implicit dual time-stepping algorithm with a time step of 10^{-6} s and 10 inner cycles. Implicit dual time-stepping is a two step process. First, a time-dependent source term is added to the residual. This source term controls the time accuracy of the solution. Second, the residual is reduced to zero while holding the physical time constant. This step is similar to the convergence of a steady state problem. Each case runs until unstart occurs or until is appears steady (10-20 ms).

6.0.5 Boundary Conditions

The boundary conditions are listed in Table 6.1. The inflow boundary condition is a user-specified flow with a boundary layer thickness corresponding to a laminar boundary layer that has been developing from the stagnation point at the bleed lip near the tunnel throat, and a uniform Mach 6.1 freestream flow. The boundary layer profile contains 50 points for the empty section and 40 points for the sections with cones, with a boundary layer thickness of 0.6 in. The profile is calculated with EDDYBL [51], assuming a stagnation pressure of 90 psia, stagnation temperature of 433 K and choked flow at the throat. The meanflow at the inflow boundary is described in 6.1.

6.0.6 Initial Conditions

The initial conditions are chosen to approximate the actual tunnel startup process. Warmbrod and Struck [49] describe the flow development in a Ludwieg tube as a two stage process consisting of an expansion wave followed by a shock wave. The rupture of the diaphragm (downstream of the test section) generates an expansion fan that propagates upstream. This induces an initial downstream flow in the test section. When the expansion fan reaches the tunnel throat, the flow at the throat becomes sonic and an approximately normal shock wave is formed in the diverging section of the nozzle and propagated downstream. The shock eventually moves to the exit of the tunnel, accelerating the flow to Mach 6 within the test section. The initial conditions in Table 6.2, along with the inflow conditions from Table 6.1, create a shock wave that propagates into the computational domain in analogy to the actual tunnel startup process. The flow behind the shock wave is the proper tunnel design flow, and is determined by the inflow boundary condition. Thus, while the initial conditions do not precisely simulate the actual tunnel starting phenomena, they qualitatively model the second stage of the startup process (in which a shock wave travels through the test section accelerating the flow to design conditions) and provide the proper test section inflow conditions for the started tunnel.

Table 6.2: Initial Conditions

		Empty Section	**Section with Cone**
Pressure	(lb/ft^2)	4.00	6.18
Temperature	(K)	29	22
Density	$(slug/ft^3)$	4.498×10^{-5}	9.000×10^{-6}
Velocity	(ft/s)	1000	1000

6.0.7 Post Processing

The geometric parameters, x and y coordinates, and the flow variables, p, ρ, M, u, v and entropy, are written to a data file every time step (*i.e.*, every 10^{-6} s) and used to create numerical schlieren images. The numerical schlieren technique [75] is a grey-scale picture with a special nonlinear scale. Numerical schlieren images are contour plots of the density

gradient along the desired plane. First, the density gradient[2] is calculated using:

$$|\nabla\rho(x,y)| = \sqrt{\left(\frac{\partial\rho}{\partial x}\right)^2 + \left(\frac{\partial\rho}{\partial y}\right)^2} \tag{6.27}$$

A special non-linear scale is determined using the following function, which is called the schlieren function:

$$Sch(x,y) = \exp\left(-c_k S(x,y)\right) \tag{6.28}$$

where

$$S(x,y) = \frac{|\nabla\rho(x,y)| - |\nabla\rho(x,y)|_0}{|\nabla\rho(x,y)|_1 - |\nabla\rho(x,y)|_0} \tag{6.29}$$

Here, $|\nabla\rho(x,y)|_0 = c_0 |\nabla\rho(x,y)|_{max}$ and $|\nabla\rho(x,y)|_1 = c_1 |\nabla\rho(x,y)|_{max}$. Choosing values for the constants is a bit of an art and depends on the maximum density gradient for each frame. Different values will improve the contrast and sharpness of the image. In general, the constants are approximately $c_0 = 0.002$, $c_1 = 0.35$ and $c_k = 0.05$. The schlieren function is then plotted in grey scale.

[2] x, y and ρ are dimensional

Chapter 7

Test Section Expansion: Results

First, the flowfield in the test section is examined with and without the 15° half-angle cone. The angle of the cone is then increased to determine the largest cone model that will fit in the tunnel without causing unstart.

7.0.8 Empty Section

Fig. 7.1 is a numerical schlieren snapshot of the flowfield after 20 ms, when the flow appears to have reached a steady state. The dark lines indicate a density gradient – e.g., shock wave, expansion fan or shear layer. Even without any model in the test section, the expansion test section generates a complex flowfield. A conical expansion fan occurs at the 45° corner and intersects the centerline. The recirculation region is separated from the core flow by a shear layer. Numerous weak shocks radiate from this shear layer and coalesce along the centerline downstream of the expansion section.

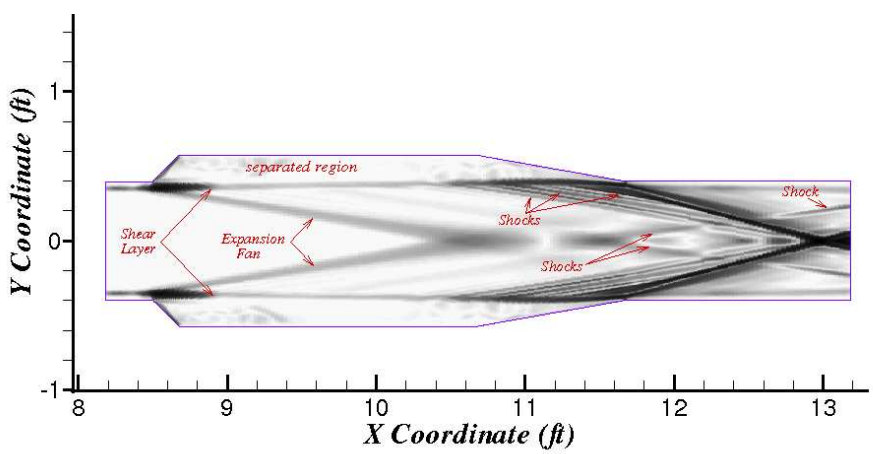

Figure 7.1: Schlieren image at $t = 20$ ms for empty test section

7.0.9 Section with 15° Cone

Fig. 7.2 shows the flowfield in the test section with a 15° half-angle cone. A shear layer appears at the 45° expansion corner and a series of shocks turn the flow back at the 10° compression corner. A recirculation region is formed in the wake of the cone and in the expansion corner (Fig. 7.3).

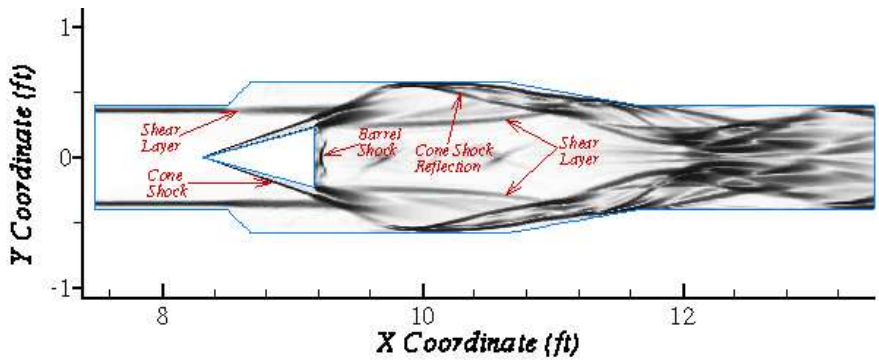

Figure 7.2: Schlieren image at $t = 20$ ms for empty test section with 15° half-angle cone

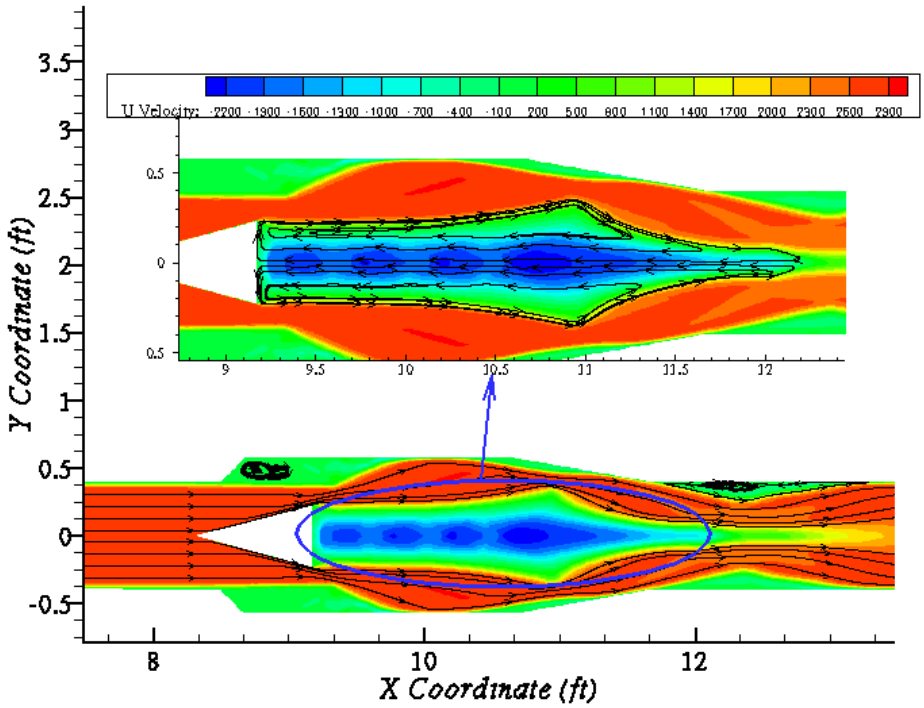

Figure 7.3: Streamlines and U-velocity (ft/s) contours in recirculation regions at $t = 20$ ms for 15° half-angle cone

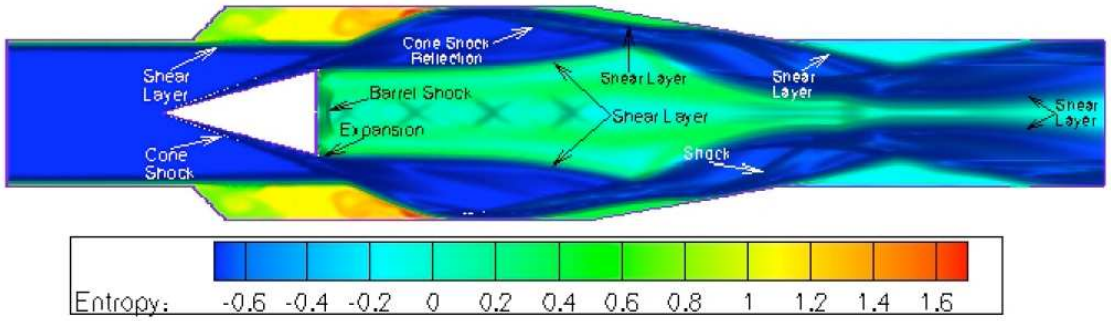

(a) Entropy

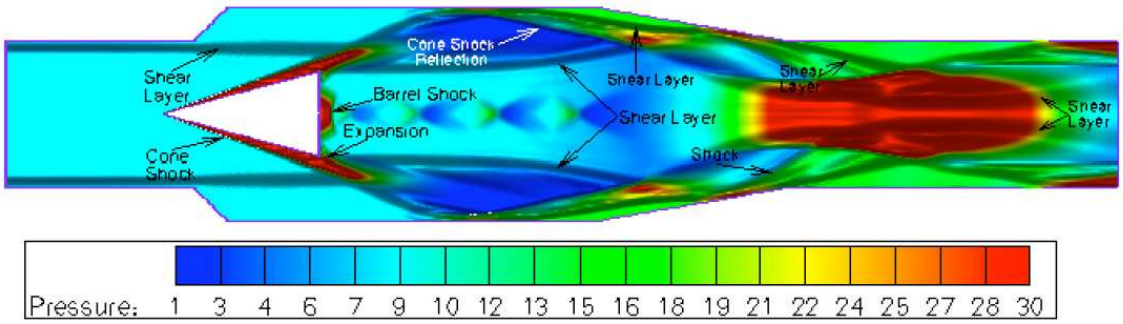

(b) Pressure (lb/ft^2)

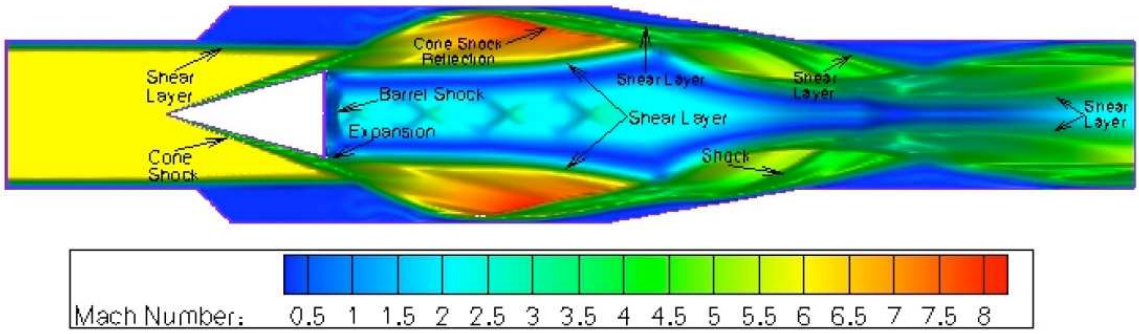

(c) Mach number

Figure 7.4: Numerical schlieren images for 15° half-angle cone at 20 ms superimposed on contour plots of (a) entropy (b) pressure and (c) Mach number

In order to distinguish between shocks, shear layers, and expansion waves, it is helpful to examine various contour plots. Entropy changes across a shear layer but not across an expansion, and there is a noticeable change across a normal shock. Pressure changes greatly across expansion fans and shocks, but only minimally across shear layers. Mach number changes across all three. The structure of the flowfield is illustrated in Figs. 7.4a-c[1] with

[1]The entropy output from GASPex in 7.4a is calculated as p/ρ^{γ}, where p and ρ are non-dimensionalized

contour plots superimposed on numerical schlieren images for the 15° half-angle cone at 20 ms.

The flow is unable to make the sharp 45° turn so a shear layer is formed and a recirculation region exists in the extended region. A series of weak shocks gradually turn the flow at the 10° compression corner so that it exits normal to the outflow boundary. As the incoming flow reaches the cone, a shock forms, which interacts first with the shear layer and then with the boundary layer along the wall. The shock reflects of the wall, providing much of the compression needed for the flow to turn the 10° corner. At the base corners of the cone there is a small expansion fan which causes the flow to expand to $M \sim 8$ (red regions in Fig. 7.4c).

A recirculation region exists behind the cone (Fig. 7.3) with a supersonic region in the center (Fig. 7.4c). The schlieren image reveals a criss-cross pattern in the wake of the cone (Fig. 7.2) and the pressure contours display a sequence of expansions and compression (blue and green contours in Fig. 7.4b). The flow is moving from right to left, towards the base of the cone, and encounters this series of expansion and compression waves. An expansion wave accelerates the flow and reflects off the bounding shear layer as a compression wave, which decelerates the flow and increases the pressure. The compression wave then reflects off the shear layer as an expansion wave. This process continues in jet-like fashion, giving rise to the criss-cross pattern. The flow is finally brought to rest by a barrel shock, which slows the flow to stagnation conditions at the cone base.

Boundary layer transition measurements on the cone surface require uniform inflow conditions upstream of the cone. Figures 7.2-7.4 indicate that the complex interactions of the shock waves, shear layers and expansions do not generate any upstream disturbances and therefore the 15° cone can be successfully tested.

---

by reference values. The range of pressures in 7.4b is limited to pressures below 30 lb/ft^2 for the purpose of distinguishing the pressure variation in the wake of the cone. The pressures in the red area downstream of the compression corner exceed 70 lb/ft^2 and a different choice of contours would illuminate variation in this region as well.

7.0.10 Section with 20° Cone

The 20° half-angle cone is shown in Fig. 7.5. This appears to be a stable configuration. There is a very small upstream influence (Fig. 7.6) where the separation bubble spreads beyond the expansion corner, but unlike with the blunter cones, this separation bubble appears to be steady and never reaches the upstream boundary. Although the tunnel is not unstarted, the noise radiating from any small oscillations of this separation bubble upstream of the corner may interfere with laminar measurements.

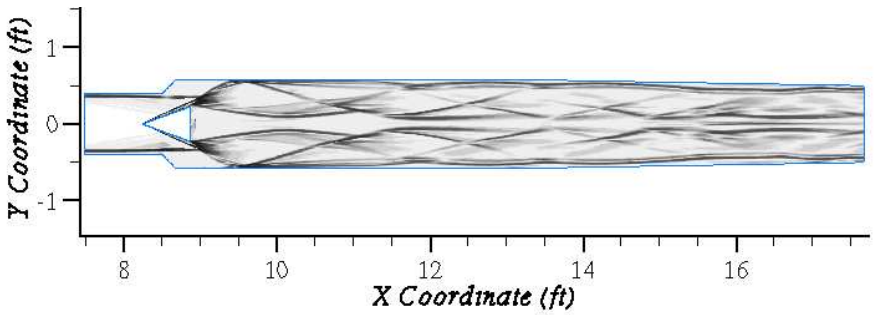

Figure 7.5: Schlieren image of developed flowfield at 9.5 ms – 20° half-angle cone

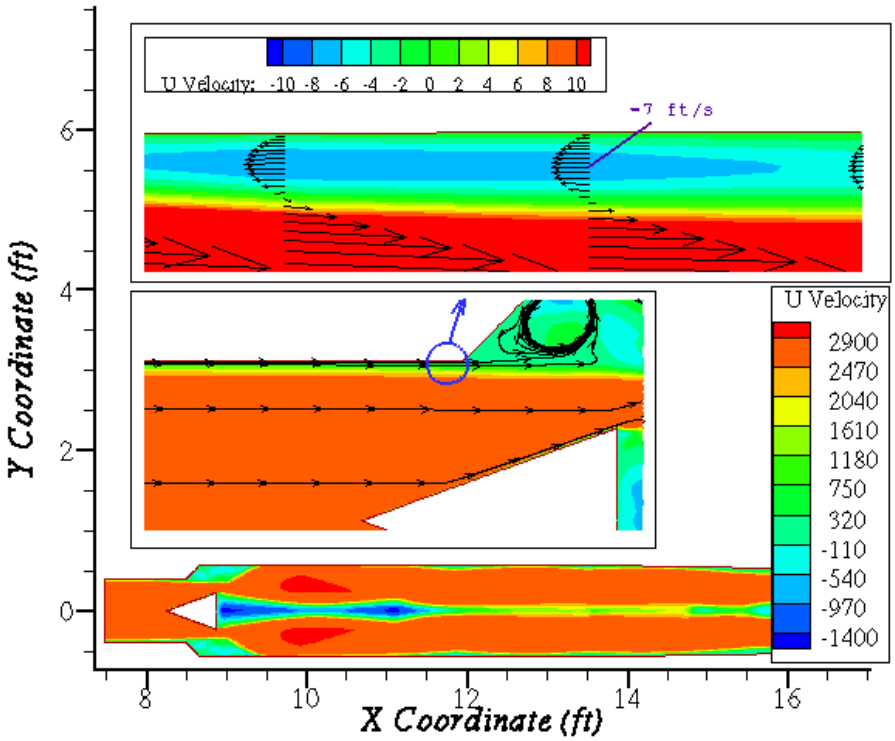

Figure 7.6: U-velocity (ft/s) contours and streamlines for the 20° half-angle cone

7.0.11 Section with 30° -75° Cones

The blunter cones appear in Figs. 7.7-7.9. A separation bubble forms at the expansion corner and bleeds out into the uniform flow. For cones with half-angles from 30° to 75°, the bubble continues to grow until it reaches the inflow boundary, unstarting the tunnel (Fig. 7.10). The U-velocity at the inflow boundary becomes negative, even though the boundary condition is trying the force the flow forward. At this point, the results cease to be meaningful and the computation is stopped.

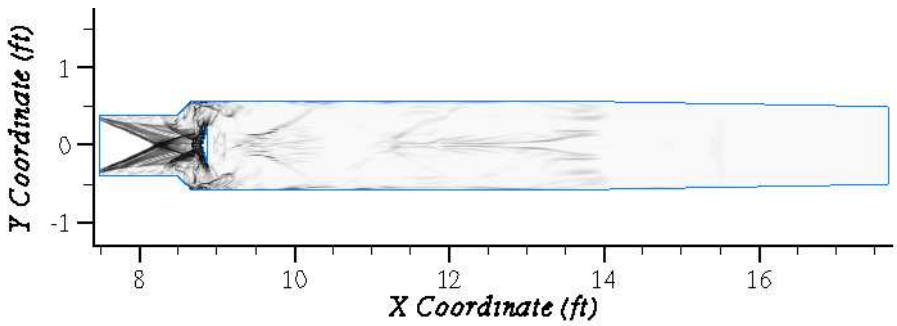

Figure 7.7: Schlieren snapshot at 3 ms – 75° half-angle cone

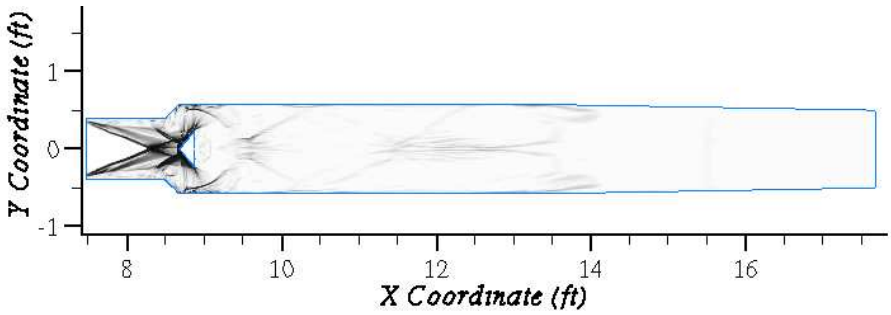

Figure 7.8: Schlieren snapshot at 3 ms – 50° half-angle cone

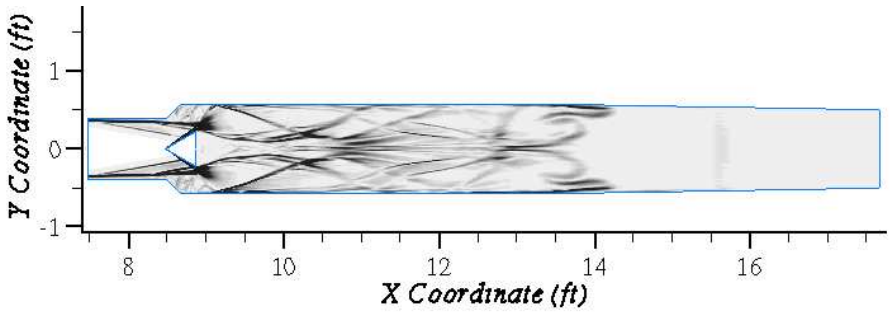

Figure 7.9: Schlieren snapshot at 3 ms – 30° half-angle cone

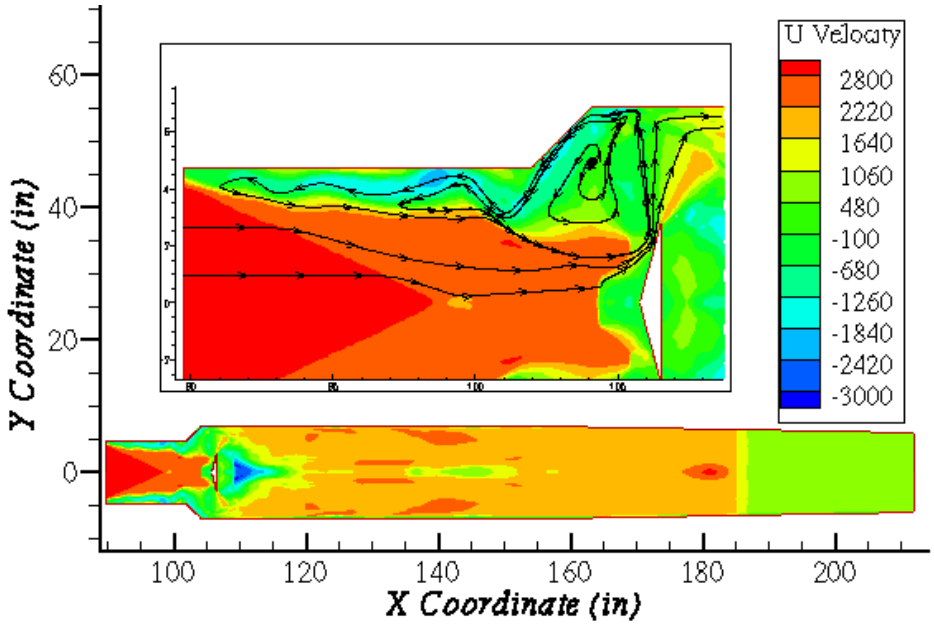

Figure 7.10: U-velocity (ft/s) contours with streamlines of 75° half-angle cone unstarting the tunnel

Chapter 8

Conclusion

Two main challenges in quiet hypersonic wind tunnels were investigated. First, a quiet supersonic nozzle was optimized to achieve the longest quiet flow test region. Second, an expansion of the test section was used to improve tunnel starting cabablities. In both cases, results were presented that would allow a larger model to be tested – the first, affecting the length of a model, and the second, affecting its bluntness and overall blockage ratio.

The first goal was to maximize the length of quiet flow in the test section by optimizing the shape of nozzle to delay boundary layer transition. A quiet Mach 6 wind tunnel nozzle was designed using an automated optimization methodology. Inviscid design, boundary layer calculations, grid generation, full Navier-Stokes solutions, and parabolized stability analysis were linked within an optimizer. Three inviscid parameters were optimized to obtain the shortest possible nozzle that does not reach $N = 6$ transition. A trade study revealed two classes of contours based on their curvature profiles. Conventional contours contained a single inflection point, whereas nozzles with compound curvature contained multiple inflection points. A response surface was created for each class of contours and a genetic algorithm was used to optimize the resulting algebraic surfaces. The Goertler instability, which is caused by concave curvature, dominated the transition process in all of the axisymmetric, hypersonic nozzles. The optimal nozzle was found to contain a slight amount of convex curvature, which helped to suppress Goertler growth. This is consistent with previous results for incompressible flow [23].

The second goal was to evaluate the startup characteristics of a proposed modification for the test section of the BAM6QT. The diameter of the test section was expanded so that shock waves from the nose of a model interacted with a shear layer before hitting the wall boundary layer, which was suggested as a way to prevent tunnel unstart in the presence

of blunt models. Several cone sizes were investigated to determine if they would unstart the tunnel. It was found that a 15° half-angle cone with fixed base diameter fit into the modified section without causing any upstream separation, but the 30° − 75° half-angle cones unstarted the tunnel. The 20° half-angle cone appeared to be stable and the separation bubble that formed in the corner moved only slightly upstream and remained in place. Even though the tunnel was not unstarted, this separation bubble may generate noise that could interfere with laminar mearsurements. This upstream effect was not evident in the 15° half-angle case, which was an improvement over the 7° half-angle cone used in the unmodified BAM6QT test section.

Appendix A

Input File for Sivells

sivells_m6 0

1.400 1716.563 1.000 1.000 1.000 1.000 0.000 1000.000

2.000 7.000 0.000 2.500 6.000 0.000 0.000 10.000

81 41 0 10 0 81 97 120 99 0 -1 0 10 0 -41 19

Appendix B

Input File for EDDYBL

IUNIT1 = 2

IUNIT2 = 7

IUNIT3 = 8

IUNIT4 = 9

IUNIT5 = 10

IUPLOT = 11

IUTYPE = 0

MODEL = -1

NVISC = 0

ALPHA = 5.198333E-01

BETA = 7.200000E-02

BETAS = 9.000000E-02

SIGMA = 5.000000E-01

SIGMAS = 5.000000E-01

PRT = 8.900000E-01

CEPS1 = 3.000000E-01

CEPS2 = 1.000000E+00

CMU = 1.600000E+00

SIGMAE = 1.680000E-02

SIGMAK = 3.000000E-01

PSIEPS = 2.600000E+01

ALPHAH = 7.745455E-01

BETAH = 1.963636E-01

GAMMAH = 4.945454E-01

CC1 = 1.800000E+00

XIS = 0.000000E+00

XMT0 = 2.500000E-01

CONE = 0.000000E+00

DS = 1.000000E-05

G = 1.400000E+00

PR = 7.200000E-01

PT1 = 2.160000E+04

R = 1.716000E+03

REK = 1.000000E+00

RMI0 = 5.912702E-02

SGN = -1.000000E+00

SSTOP = 1.555900E+01

SU = 1.985999E+02

TT1 = 7.794000E+02

USTOP = 0.000000E+00

VISCON = 2.270000E-08

VISPOW = 1.500000E+00

WAVE = 0.000000E+00

XK = 1.040000E+00

XMA = 5.000000E-01

ZIOTAE = 1.000000E-06

ZIOTAL = 1.000000E-02

IBODY = 2

IBOUND = 0

IEDGE = 206

IEND1 = 999

ISHORT = 1

J = 1

KEBC = 0

KODWAL = 2

MSTART = 2

NFLAG = 1

NUMBER = 500

PROVAL(1) = 1.000000E+10

PROVAL(2) = 1.000000E+10

PROVAL(3) = 1.000000E+10

PROVAL(4) = 1.000000E+10

PROVAL(5) = 1.000000E+10

PROVAL(6) = 1.000000E+10

PROVAL(7) = 1.000000E+10

PROVAL(8) = 1.000000E+10

PROVAL(9) = 1.000000E+10

PROVAL(10)= 1.000000E+10

ALAMM = 1.000000E+00

CF = 4.566321E-02

DELTA = 3.954203E-06

H = 4.600000E+00

R2D = 1.000000E+00

RETHET = 2.460000E+01

SI = 1.000000E-05

Appendix C

Input File for STABL

```
#!/usr/bin/perl
# ***************************************************************
# PSE-Chem linear batch script generated automatically
# ***************************************************************
use strict;
use Psechem_scripting;
# Create a new Psechem scripting object
my $pse= Psechem_scripting⇒new(-mean_flow_file⇒"stabl_meanflow.psx");
# Set the output directory
$pse⇒output_dir("PSE_results");
# General STABL settings
$pse⇒runtime_env(STABL_BL_IMET ⇒"3",
STABL_BL_JMAX ⇒"-1",
STABL_BL_JMIN ⇒"4",
STABL_BL_RBL ⇒"0.995",
STABL_SH_DETDPM ⇒"0.02",
STABL_SH_DETJMP ⇒"0",
STABL_SH_DETVAR ⇒"Default");
# Set MPI parameters if needed
$pse⇒mpi_params(-mpirun⇒" /stabl/lam-mpi-pgi/bin/mpirun",
-np⇒47);
# Set PSE parameters if needed
$pse⇒pse_params(iaxi⇒"1",
```

```
ichem⇒“0”,
ishock_method⇒“1”,
ivib⇒“0”);
#2D second mode
$pse⇒pse_batch_add_mat(-betas⇒“0”,
-omegas⇒“5-90;22”,
-slocs⇒“0.1- 4.4 ;90”,
-title⇒“Row 1”);
$pse⇒pse_batch_add_mat(-betas⇒“0”,
-omegas⇒“100-500;30”,
-slocs⇒“0.1- 4.4 ;90”,
-title⇒“Row 2”);
#PSE-Chem solver in batch mode on these cases
$pse⇒run_psechem();
exit;
```

Appendix D

Input File for LASTRAC

```
// sample input file for lastrac for Gortler instability
num_normal_pts = 101
strm_curvt = true //must turn on streamwise curvature for Gortler
transv_curvt = true //cannot ignore transverse curvature if using
//integer azimuthal wave number, nwave_axisym_beta
use_extrap_mprof = false // Navier-Stoke mean flow, avoid extrapolation
mflow_filename = "./meanflow.out"
mflow_storage_type = memory_storage
marching_method_2d = along_station
init_station = 333
final_station = 700
solution_type = marching_pse_solution
freq_unit = in_hertz_freq
beta_unit = nwave_axisym_beta //using integer azimuthal wavenumber
// Gortler modes are steady state (zero frequency)
// use a very small value for frequency
freq = 32*1.e-4
beta = 35,40,45,50,55,60,65,70,75,80,
85,90,95,100,105,110,115,120,130,140,
145,150,155,160,165,170,175,180,185,190,200,210
// allows a small negative cr for gortler
cr_min = -0.004, cr_max = 1.2
wall_dpdy_ratio_min = 1.e-12 //mean flow a little noisy, this is necessary
```

```
//to avoid filtering out a good mode
np_growth_rate_min = -0.01 //accept stable modes (check the manual)
alpha_i_max = 0.01 //filter out upstream modes with large growth rates
//qp_approx = true
pns_approx = true // avoid numerical instability due to small step size
use_l2alpha = false //don't use l2alpha for noisy meanflow
output_eigenfunction = true
```

Appendix E

Response Surface Code for Conventional Contours

```
/*— modeFRONTIER Response Surface ————————-
Code Created by
modeFRONTIER - (c) ES.TEC.O srl
modeFRONTIER Version modeFRONTIER 4.0 b20071211
Date Mon Sep 15 17:53:40 EDT 2008
Project Name rsm_conventional
Operating System Linux 2.6.18-6-amd64 i386
Java (SDK/JRE) Version 1.6.0_01
Java Vendor Sun Microsystems Inc.
Java Vendor URL http://java.sun.com/
User Name hadassah */
/*————————————————————————————
x[0] corresponds to variable length
x[1] corresponds to variable max_curv
————————————————————————————————*/
/*————————————————————————————
Response Surface Name : L_quiet_SVD_0
Response Surface Type : Polynomial SVD
————————————————————————————————*/
#include <stdio.h>
#include <stdlib.h>
#include <math.h>
#include <string.h>
```

```
void svd(double x[], double *y);
int main(){
double x[3];
double *y;
x[0]= 4.715e+00; /* input 1: axial length */
x[1]= -1.869e-02; /* input 2: maximum concave (negative) curvature */
svd(x,y);
exit(0);}
void svd(double x[], double *y){
// SVD data
const double xRange[2][2] = {
{ 1.488524, 4.720294},
{ -0.29456633858267717, -0.01879442913385827};}
const double yRange[2] = { 8.01496781077729, 53.8};
const int alpha[3][3] = {
{ 0, 0},
{ 1, 0},
{ 0, 1}
};
const double b[3] = { -0.03536767819914001, 0.6640549682306915, 0.3055029381760977};
int i, j, k;
double xn[2];
double yn, yy;
double basis;
double point[2];
// normalize input
for (i=0; i<2; i++) {
xn[i] = (x[i]-xRange[i][0])/(xRange[i][1]-xRange[i][0]);}
// perform computations
yn = 0.0;
```

```
for (i=0; i<3; i++) {
basis = b[i];
for (j=0; j<2; j++) {
for (k=1; k≤alpha[i][j]; k++) {
basis *= xn[j];}}
yn += basis;}
// scale output
yy = yRange[0]+(yRange[1]-yRange[0])*yn;
// *y = yy;
printf("L_quiet based on SVD: %f m.",yy);
return;
}
```

References

[1] Juliano, T.J., Schneider, S.P., Aradag, S., Knight, D.D.: Quiet-flow Ludwieg tube for hypersonic transition research. AIAA Journal **46**(7), 1757–1763 (2008)

[2] Craddock, C.S.: Computational optimization of scramjets and shock tunnel nozzles. Ph.D. thesis, The University of Queensland, Brisbane, Australia (1999)

[3] Sivells, J.: A computer program for the aerodynamic design of axisymmetric and planar nozzles for supersonic and hypersonic wind tunnels. Arnold Engineering Development Center, AEDC-TR-73-168 (1973)

[4] Schneider, S.P.: Design and fabrication of a 9.5-inch Mach-6 quiet-flow Ludwieg tube. 20th AIAA Advanced Measurement and Ground Testing Technology Conference, AIAA Paper No. 1998-2511 (1998)

[5] Schneider, S.P.: Hypersonic laminar-turbulent transition on circular cones and scramjet forebodies. Progress in Aerospace Sciences **40**(1), 1–50 (2004)

[6] Beckwith, I.E., Chen, F.J., Creel, T.R.: Design requirements for the NASA Langley supersonic low disturbance wind tunnel. 14th Aerodynamic Testing Conference, AIAA Paper No. 1986–0763 (1986)

[7] Reed, H., Kimmel, R., Schneider, S., Arnal, D.: Drag prediction and transition in hypersonic flow. 28th AIAA Fluid Dynamics Conference, AIAA Paper No. 1997–1818 (1997)

[8] Schneider, S.P.: The development of hypersonic quiet tunnels. 37th AIAA Fluid Dynamics Conference, AIAA Paper No. 2007–4486 (2007)

[9] Schneider, S.P., Juliano, T.J., Borg, M.P.: High Reynolds-number laminar flow in the Mach-6 quiet-flow Ludwieg tube. 36th AIAA Fluid Dynamics Conference, AIAA Paper No. 2006–3056 (2006)

[10] Saric, W.S.: Physical description of boundary-layer transition: Experimental evidence. In: AGARD Report 793, Special Course on Progress in Transition Modelling, pp. 1/1–1/51. AGARD (1994)

[11] Arnal, D.: Boundary layer transition: Predictions based on linear theory. In: AGARD Report 793, Special Course on Progress in Transition Modelling, pp. 2/1–2/63. AGARD (1994)

[12] Herbert, T.: Parabolized stability equations. In: AGARD Report 793, Special Course on Progress in Transition Modelling, pp. 4/1–4/34. AGARD (1994)

[13] Reed, H.: Direct numerical simulation of transition: The spatial approach. In: AGARD Report 793, Special Course on Progress in Transition Modelling, pp. 4/1–4/46. AGARD (1994)

[14] Saric, W.S., Reed, H.L., White, E.B.: Stability and transition of three-dimensional boundary layers. Annual Review of Fluid Mechanics **35**, 413–440 (2003)

[15] Mack, L.M.: Boundary-layer stability theory. California Institute of Technology, Jet Propulsion Laboratory, Document 900-277(Rev. A.) (1969)

[16] Erlebacher, G., Hussaini, M.Y.: Non linear evolution of a second mode wave in supersonic boundary layers. Applied Numerical Mathematics **7**(1), 73–91 (1991)

[17] Gajjar, J.S.B.: Amplitude-dependent neutral modes in compressible boundary layer flows. NASA TM-102524 (1990)

[18] Estorf, M., Radespiel, R., Schneider, S.P., Johnson, H.B., Hein, S.: Surface-pressure measurements of second-mode instability in quiet hypersonic flow. 46th AIAA Aerospace Sciences Meeting and Exhibit,, AIAA Paper No. 2008–1153 (2008)

[19] McKeel, S.A.: Numerical simulation of the transition region in hypersonic flow. Ph.D. thesis, Virginia Polytechnic Institute and State University (1996)

[20] Johnson, H.B.: Thermochemical interactions in hypersonic boundary layer stability. Ph.D. thesis, University of Minnesota (2000)

[21] Herbert, T.: Parabolized stability equations. Annual Review of Fluid Mechanics **29**, 245–283 (1997)

[22] Saric, W.S.: Gortler vortices. Annual Review of Fluid Mechanics **26**, 379–409 (1994)

[23] Banmalek, A., Saric, W.S.: Effects of curvature variations on the nonlinear evolution of goertler vortices. Physics of Fluids **6**(10), 3353–3367 (1994)

[24] Whang, C.W., Zhong, X.: Direct numerical simulation of goertler instability in hypersonic boundary layers. 37th AIAA Aerospace Sciences Meeting and Exhibit, AIAA Paper No. 1999–0291 (1999)

[25] Goulpie, P., Klingmann, B.G.B., Bottaro, A.: Gortler vortices in boundary layers with streamwise pressure gradient: Linear theory. Physics of Fluids **8**(2), 451–459 (1996)

[26] Langlois, M., Casalis, G., Arnal, D.: On the practical application of the PSE approach to linear stability analysis. Aerospace Science and Technology, **3**, 167–176 (1998)

[27] Chang, C.L., Malik, M.R.: Compressible stability of growing boundary layers using parabolized stability equations. 22nd AIAA Fluid Dynamics, Plasma Dynamics & Lasers Conference, AIAA Paper No. 1991–1636 (1991)

[28] Stanek, M.J., Rubin, S.B.: A high-oder reduced navier stokes approximation for accurate mean flow calculation. 35th AIAA Aerospace Sciences Meeting and Exhibit, AIAA Paper No. 1996–0543 (1997)

[29] Schneider, S.P.: Design of a Mach-6 quiet-flow wind-tunnel nozzle using the e**N method for transition estimation. 36th AIAA Aerospace Sciences Meeting Meeting, AIAA Paper No. 1998-0547 (1998)

[30] Juliano, T.J., Swanson, E.O., Schneider, S.P.: Transition research and improved performance in the Boeing/AFOSR Mach-6 quiet tunnel. 45th AIAA Aerospace Sciences Meeting and Exhibit, AIAA Paper No. 2007–0535 (2007)

[31] Coleman, C.P.: Boundary layer transition in the leading edge region of a swept cylinder in high speed flow. NASA TM 1998-112224 (1998)

[32] Pate, S.R.: Effects of wind tunnel disturbances on boundary-layer transition with emphasis on radiated noise: A review. 11th Aerodynamic Testing Conference, AIAA Paper No. 1980–0431 (1980)

[33] Chen, F., Malik, M.R.: Instabilities and transition in the wall boundary layers of low-disturbance supersonic nozzles. 18th AIAA Fluid Dynamics, Plasma Dynamics & Lasers Conference, AIAA Paper No. 1985–1573 (1985)

[34] Beckwith, I.E., Malik, M.R., Chen, F.J.: Nozzle optimization study for quiet supersonic wind tunnels. 17th AIAA Fluid Dynamics, Plasma Dynamics & Lasers Conference, AIAA Paper No. 1984-1628 (1984)

[35] Shukla, V., Gelsey, A., Schwabacher, M., Smith, D., Knight, D.D.: Automated redesign of the NASA P8 hypersonic inlet using numerical optimization. 32nd Joint Propulsion Conference, AIAA Paper No. 1996–2549 (1996)

[36] Xu, X., Dajun, X., Guobiao, C.: Optimization design for scramjet and analysis of its operation performance. Acto Astronautica **57**, 390–403 (2005)

[37] Amoignon, O., Pralits, J., Hanifi, A., Berggren, M., Henningson, D.: Shape optimization for delay of laminar-turbulent transition. AIAA Journal **44**(5), 1009–1024 (2006)

[38] Hogberg, M.: Optimal control of boundary layer transition. Ph.D. thesis, Royal Institute of Technology, Stockholm, Sweden (2001)

[39] Davey, M.G.: A hypersonic nozzle for the X3 expansion tube. Bachelor of Engineering Thesis, The University of Queensland, Brisbane, Australia (2006)

[40] Korte, J.J.: Inviscid design of hypersonic wind tunnel nozzles for a real gas. 38th AIAA Aerospace Sciences Meeting Meeting, AIAA Paper No. 2000–0677 (2000)

[41] Chadwick, K.M., Holden, M.S., Korte, J.J., Anderson, E.C.: Design and fabrication of a Mach 8 contoured nozzle for the LENS facility. 34th AIAA Aerospace Sciences Meeting Meeting, AIAA Paper No. 1996–0585 (1996)

[42] Schneider, S.P.: A quiet flow Ludwieg tube for study of transition in compressible bounary layers; design and feasibility. Semiannual Status Report for NASA Grant NAG-1-1133, NASA CR–187374 (1990)

[43] Schneider, S.P.: Development of quiet-flow supersonic wind tunnels for laminar-turbulent transition research. Final Report for NASA Grant NAG-1-1133, NASA CR-197286 (1994)

[44] Seablom, K.D., Soeder, R.H., Stark, D.E., Leone, J.F.X., Henry, M.W.: NASA Glenn 1-by-1 foot supersonic wind tunnel user manual. NASA Glenn Research Center, NASA TM 1999–208478 (1999)

[45] Reichenau, D.E.A.: Investigation of an attached inflatable decelerator for drag augmentation of the Voyager entry capsule at supersonic speeds. Arnold Engineering Development Center, AEDC-TR-68-71 (1968)

[46] Petty, J.S.: Wind tunnel tests of a new diffuser concept. Aerospace Research Laboratories, TR 75-0198 (1975)

[47] Juliano, T.J., Segura, R., Borg, M.P., Casper, K., Hannon, M.J.J., Wheaton, B.M., Schneider, S.P.: Starting issues and forward-facing cavity resonance in a hypersonic quiet tunnel. 38th AIAA Fluid Dynamics Conference and Exhibit, AIAA Paper No. 2008–3735 (2008)

[48] Holland, S.D., Hodge, J.S., Perkins, J.N.: Wind tunnel blockage study of a generic three-dimensional sidewall compression scramjet inlet at Mach 10. 29th Aerospace Sciences Meeting, AIAA Paper No. 1991-0294 (1991)

[49] Warmbrod, J.D., Struck, H.G.: Application of the characteristic method in calculating the time dependent, one-dimensional, compressible flow in a tube wind tunnel. NASA George C. Marshall Space Flight Center, NASA TM X-53769 (1968)

[50] Schneider, S.P., Juliano, T.J.: Laminar-turbulent transition measurements in the Boeing/AFOSR Mach-6 quiet tunnel. 37th AIAA Fluid Dynamics Conference and Exhibit, AIAA Paper No. 2007–4489 (2007)

[51] Wilcox, D.C.: Turbulence Modeling For CFD. DCW Industries Inc., La Canada, CA (1993)

[52] Casper, K.M., Wheaton, B.M., Johnson, H.B., Schneider, S.P.: Effect of freestream noise on roughness-induced transition at Mach 6. 38th AIAA Fluid Dynamics Conference and Exhibit, AIAA Paper No. 2008-4291 (2008)

[53] Chen, F.J., Wilkinson, S.P., Beckwith, I.E.: Gortler instability and hypersonic quiet nozzle design. 22nd AIAA Fluid Dynamics, Plasma Dynamics & Lasers Conference, AIAA Paper No. 1991-1648 (1991)

[54] Program Development Corporation, White Plains, NY: GridPro/az3000 User's Guide and Reference Manual (1998)

[55] Aerosoft Inc., http://www.aerosft.com: General Aerodynamic Simulation Program User Manual (2004)

[56] Jentik, T.N.: CFD code validation for nozzle flowfields. 27th Joint Propulsion Conference, AIAA Paper No. 1991–2565 (1991)

[57] Knight, D.: Elements of Numerical Methods for Compressible Flows. Cambridge University Press, New York (2006)

[58] Van Leer, B.: Flux vector splitting for the Euler equations. 8th International Conference on Numerical Methods in Fluid Dynamics **170**, 507–512 (1982)

[59] Hirsch, C.: Numerical Computation of Internal and External Flows, Volume 2: Computational Methods for Inviscid and Viscous Flows, vol. 2. John Wiley & Sons, Chichester, England (1990)

[60] Robarge, T.W.: Laminar boundary-layer instabilities on hypersonic cones: Computations for benchmark experiments. Ph.D. thesis, Purdue University (2005)

[61] Muramoto, K.K.: Algebraic correlations for high-speed transition prediction on sharp and blunt cones. 37th AIAA Aerospace Sciences Meeting and Exhibit, AIAA Paper No. 1999–0405 (1999)

[62] Johnson, H.B., Candler, G.V.: Hypersonic boundary layer stability analysis using psechem. 35th AIAA Fluid Dynamics Conference and Exhibit, AIAA Paper No. 2005–5023 (2005)

[63] Malik, M.R.: e**Malik: A new spatial stability analysis program for transition prediction using the e**N method. High Technology Corporation, HTC-8902 (1989)

[64] Johnson, H.B., Alba, C.R., Candler, G.V., MacLean, M., Wadhams, T., Holden, M.: Boundary layer stability analysis to support the HIFiRE transition experiment. 45th AIAA Aerospace Sciences Meeting and Exhibit, AIAA Paper No. 2007–0311 (2007)

[65] Johnson, H.B.: STABL Stability and Transition Analysis for Hypersonic Boundary Layers Program Reference. University of Minnesota, stabl 2.8 edn. (2007)

[66] Mack, L.M.: Stability of axisymmetric boundary layers on sharp cones at hypersonic Mach numbers. 19th AIAA Fluid Dynamics, Plasma Dynamics & Lasers Conference,, AIAA Paper No. 1987-1413 (1987)

[67] Stetson, K.F.: Mach 6 experiments of transition on a cone at angle of attack. Journal of Spacecraft and Rockets **19**(5), 397–403 (1982)

[68] Chen, F.J., Malik, M.R., Beckwith, I.E.: Advanced Mach-3.5 axisymmetric quiet nozzle. 21st Fluid Dynamics, Plasma Dynamics and Lasers Conference, AIAA Paper No. 1990-1592 (1990)

[69] Chen, F.J., Malik, M.R., Beckwith, I.E.: Gortler instability and supersonic nozzle design. AIAA Journal **30**(8), 2093–2094 (1992)

[70] Chang, C.L.: Langley stability and transition analysis code (LASTRAC) version 1.2 user manual. NASA Langley Research Center, NASA TM 2004-213233 (2004)

[71] modeFRONTIER: Multi-Objective Optimization and Design Environment. URL http://www.esteco.com/products.jsp

[72] Schneider, S.P.: Laminar-turbulent transition on reentry capsules and planetary probes. Journal of Spacecraft and Rockets **43**, 1153–1173 (2006)

[73] Skoch, C., Schneider, S.P., Borg, M.P.: Disturbances from shock/boundary-layer interactions affecting upstream hypersonic flow. 35th AIAA Fluid Dynamics Conference, AIAA Paper No. 2005-4897 (2005)

[74] Rae, W.H.J., Pope, A.: Low-Speed Wind Tunnel Testing, 2nd edn. John Wiley & Sons, New York (1965)

[75] Aradag, S., Knight, D.: Simulation of supersonic flow over a cavity. 43rd AIAA Aerospace Sciences Meeting, AIAA Paper No. 2005-0848 (2005)

Vita

Hadassah Naiman

Education

2003 BS in Physics, Minors in Biology, Chemistry, Mathematics, Loyola University Chicago, Chicago, Illinois.

2006 MS in Mechanical and Aerospace Engineering, Rutgers, The State University of New Jersey, New Brunswick, New Jersey.

2010 PhD in Mechanical and Aerospace Engineering, Rutgers, The State University of New Jersey, New Brunswick, New Jersey.

Work Experience

2003-08 *Graduate Assistant*, Department of Mechanical and Aerospace Engineering, Rutgers, The State University of New Jersey, New Brunswick, New Jersey.

2008-10 *Research Scientist*, Combustion Research and Flow Technology, Inc. Pipersville, Pennsylvania.

Publications

2006 Naiman, H., Knight, D. *The Effect of Reynolds Number on Shock Interaction with a Rigid, Porous Barrier.* AIAA 44th Aerospace Sciences Meeting and Exhibit, Reno, NV. AIAA Paper No. 2006-1301, January.

2007 Naiman, H., Knight D. *The Effect of Porosity on Shock Interactions with a Rigid, Porous Barrier.* Shock Waves **16**, pp. 321-337.

2007 Naiman, H., Knight, D., Aradag, S., Juliano, T., Schneider, S. *Performance Improvements in Boeing/AFOSR Mach 6 Quiet Wind Tunnel Based on CFD Predictions.* 3rd International Symposium on Integrating CFD and Experiments in Aerodynamics, Colorado Springs, CO, June.

2007 Naiman, H., Knight, D. *Computational Redesign of the Test Section for the Boeing/AFOSR Mach 6 Quiet Tunnel.* 2nd European Conference for Aerospace Sciences (EUCASS), Brussels, Belgium, July.

2009 Naiman, H., Knight, D., Schneider, S. *Computational Redesign of the Test Section for the Boeing/AFOSR Mach 6 Quiet Tunnel.* Proceedings of the Institution of Mechanical Engineers, Part G: Journal of Aerospace Engineering **223**(4), pp. 407-413.